



**HAL**  
open science

# Quantitative evolution of the petrophysical properties of andesites affected by argillic alteration in the hydrothermal system of Petite Anse-Diamant, Martinique

Charli Delayre, Patricia Patrier Mas, Paul Sardini, Philippe Cosenza, Anthony Thomas

## ► To cite this version:

Charli Delayre, Patricia Patrier Mas, Paul Sardini, Philippe Cosenza, Anthony Thomas. Quantitative evolution of the petrophysical properties of andesites affected by argillic alteration in the hydrothermal system of Petite Anse-Diamant, Martinique. *Journal of Volcanology and Geothermal Research*, 2020, 401, pp.106927 -. 10.1016/j.jvolgeores.2020.106927 . hal-03492252

**HAL Id: hal-03492252**

**<https://hal.science/hal-03492252v1>**

Submitted on 15 Jul 2022

**HAL** is a multi-disciplinary open access archive for the deposit and dissemination of scientific research documents, whether they are published or not. The documents may come from teaching and research institutions in France or abroad, or from public or private research centers.

L'archive ouverte pluridisciplinaire **HAL**, est destinée au dépôt et à la diffusion de documents scientifiques de niveau recherche, publiés ou non, émanant des établissements d'enseignement et de recherche français ou étrangers, des laboratoires publics ou privés.



Distributed under a Creative Commons Attribution - NonCommercial 4.0 International License

1  
2  
3  
4  
5  
6  
7  
8  
9  
10  
11  
12  
13  
14  
15  
16  
17  
18  
19  
20  
21  
22  
23  
24  
25  
26  
27  
28

**Quantitative evolution of the petrophysical properties of andesites  
affected by argillic alteration in the hydrothermal system  
of Petite Anse-Diamant, Martinique**

Charli DELAYRE<sup>a</sup>, Patricia PATRIER MAS<sup>a</sup>, Paul SARDINI<sup>a</sup>, Philippe COSENZA<sup>a,\*</sup>, Anthony THOMAS<sup>b</sup>

<sup>a</sup>University of Poitiers, UMR CNRS 7285 IC2MP- HydrASA, ENSI Poitiers, France.

<sup>b</sup>University of Poitiers - ISAE-ENSMA, Institut PPRIME, UPR 3346 CNRS, ENSI Poitiers Chasseneuil, France.

**\*Corresponding author**

Philippe COSENZA

Ecole Nationale Supérieure d'Ingénieurs de Poitiers  
Université de Poitiers-CNRS  
1 rue Marcel Doré, Bat B1  
TSA 41105  
86073 Poitiers cedex 09  
France  
Email: philippe.cosenza@univ-poitiers.fr

*Intended for publication in Journal of Volcanology and Geothermal Research*

29 **Abstract**

30 The evolution of the petrophysical properties of rocks induced by hydrothermal alteration is  
31 often considered qualitatively by sorting the hydrothermal alterations encountered from low  
32 to high intensity, depending on the identified mineral paragenesis. In this paper, we studied  
33 the evolution of three different petrophysical properties (connected porosity, permeability and  
34 electrical conductivity) as a function of the argillization degree of andesites affected by  
35 argillic alteration identified in the caprock formation of the Petite Anse-Diamant  
36 hydrothermal system in Martinique. These petrophysical measurements were supplemented  
37 by quantitative mineral evaluation via scanning electron microscopy (i.e., the Quantitative  
38 Evaluation of Minerals by Scanning electron microscopy or the QEMSCAN® method),  
39 connected porosity mapping using  $^{14}\text{C}$ -PMMA method and measurements of methylene blue  
40 (MB) values and structural water proportions ( $\text{H}_2\text{O}^+$ ). In the series of rocks investigated, an  
41 increasing trend of clay mineral abundances (montmorillonite and kaolinite) from 5.68 to  
42 37.56 % was revealed by the QEMSCAN® method. Based on the quantitative results, the  
43 structural water proportions were used as a proxy of argillic alteration progression.  
44 Comparison between the mineral maps provided by the QEMSCAN® system and connected  
45 porosity mapping observed in autoradiographs using  $^{14}\text{C}$ -PMMA method revealed a good  
46 correlation with clay mineral phases, dissolution vugs and fractures. The connected porosities  
47 evaluated with the triple weight method range from 3.74 to 35.35 % and show a good  
48 correlation ( $R^2 = 0.8835$ ) with the  $\text{H}_2\text{O}^+$  values, revealing that porosity development is mainly  
49 due to the replacement of primary phases by clay minerals. In contrast, the crystallization of  
50 silica, carbonates and, to a lesser extent, iron oxides tends to clog connected pores, inducing a  
51 local decrease in connected porosity, as revealed in autoradiographs. The Darcian  
52 permeability ranges from  $7.66 \cdot 10^{-20}$  to  $5.36 \cdot 10^{-17}$   $\text{m}^2$  and shows a moderate correlation with  
53 the connected porosity. The bulk electrical conductivity measured as a function of the

54 conductivity of the saturating solution reveals the significant contribution of surface  
55 conduction arising from montmorillonite. At a pore fluid salinity of 2 wt % (the salinity of the  
56 Eaux Ferrées thermal spring), the bulk electrical conductivity shows a relatively good  
57 correlation with the  $H_2O^+$  values ( $R^2=0.8591$ ) and an even better correlation with the MB  
58 values ( $R^2=0.9579$ ). The contribution of montmorillonite to the bulk electrical conductivity  
59 was estimated with the use of the isoconductivity point, showing an increase in the BM values  
60 and a strong correlation ( $R^2= 0.9806$ ).

61 **Keywords:** argillic alteration, petrophysical properties, autoradiography, porosity,  
62 permeability, electrical conductivity, Petite Anse-Diamant hydrothermal system, Martinique.

63

## 64 **1. Introduction**

65 Geothermal energy has been of increasing interest in recent decades, notably due to its  
66 environmentally friendly character with regard to the low carbon dioxide emissions per kWh  
67 produced by geothermal power plants (Kagel and Gawell 2005). In comparison with other  
68 energy sources, geothermal energy provides a base load power that is not subject to  
69 environmental variables such as sunshine or wind, as are photovoltaic and wind technologies.  
70 On the other hand, the main limitations for the development of geothermal power plants are  
71 the availability and the capacity of efficiently targeting geological areas with a sufficient local  
72 temperature gradient and fluid circulation. These limiting factors could be overcome with the  
73 development of enhanced geothermal systems (EGS), seen as the future of geothermal energy  
74 by several authors (Tester et al. 2006; Rybach 2010; Gerber and Maréchal 2012). Until this  
75 technology is fully operational, the success of finding new geothermal fields is reliant on  
76 exploration work intrinsically based on a cross-disciplinary approach with geological,  
77 geochemical and geophysical surveys.

78 Inherent to geothermal systems, hydrothermal alterations are the result of fluid/rock  
79 interactions inducing the dissolution of primary minerals of the host rocks and/or the  
80 crystallization of a wide range of minerals depending on several factors such as the fluid/rock  
81 ratio, time, temperature, pressure, fluid chemistry and permeability (Browne 1978; Roberson  
82 and Lahann 1981; Beaufort et al. 1992; Inoue 1995; Patrier et al. 1996; Meunier et al. 2017).  
83 Such dissolution and crystallization processes lead to the modification of petrophysical  
84 properties such as porosity and permeability, which are essential for the understanding of the  
85 hydrogeological dynamics of hydrothermal systems, and in a more practical way, to predict  
86 the geothermal reservoir behaviour during exploitation (Pruess 1990; O'Sullivan et al. 2001).  
87 Prospecting tools such as electrical and electromagnetic (EM) methods are commonly used  
88 for the characterization of geothermal settings as well as to target high-conductivity anomalies

89 of the subsurface (Komori et al. 2010; Gonzales et al. 2014; Muñoz 2014; Revil et al., 2018a;  
90 2018b; Ahmed et al. 2018; Lévy et al., 2018; Gailler et al., 2019). These anomalies are  
91 generally related to the presence of clay minerals resulting from fluid/rock interactions and  
92 constitute the so-called caprock formation of hydrothermal systems. The associated high  
93 conductivity results from the high cation exchange capacity (CEC) of these minerals,  
94 particularly of smectite minerals exhibiting a large amount of cations adsorbed onto their  
95 platelet surfaces (e.g., Lévy et al., 2018). However, as Muñoz (2014) reported, the high-  
96 conductivity anomalies observed in the field do not always indicate the presence of a caprock  
97 and can lead to the incorrect targeting of geothermal wells. Thus, we understand that upfront  
98 costs as well as the risk related to the drilling of unproductive wells have a determinant  
99 impact on potential investments. Aimed at reducing the risk of unsuccessful wells, laboratory  
100 studies investigating hydrothermal alterations and their effects on petrophysical rock  
101 properties are essential to better understand the operation of hydrothermal systems and to  
102 interpret the data arising from the exploration phase. In the literature, a significant proportion  
103 of available papers focuses entirely or partially on the evolution of petrophysical properties  
104 depending on parameters such as temperature, pressure and lithology, without taking into  
105 account hydrothermal alterations (Björbsson and Bodvarsson 1990; Boitnott and Boyd 1996;  
106 Nielson et al. 1996; Dobson et al. 2003; Stimac et al. 2004). It is only recently that  
107 hydrothermal alterations are considered qualitatively in parallel with the above-cited  
108 parameters for the study of the petrophysical property evolution of volcanic rocks in  
109 hydrothermal contexts. Notably, and through several papers, Frolova et al. (2001, 2006, 2010  
110 and 2015) studied the influence of hydrothermal alterations on the petrophysical properties of  
111 rocks from the Kuril-Kamchatka island arc by dividing the hydrothermal alterations  
112 encountered into low-temperature alterations and high-temperature alterations. Mordensky et  
113 al (2019) on their side focused their study on high temperature hydrothermal alterations

114 developed in Rotokawa geothermal field. Nevertheless, hydrothermal alterations are sorted  
115 from weak to high depending on the mineral paragenesis identified usually through optical  
116 microscopy observation (Kristinsdóttir et al. 2010; Wyring et al. 2014; Mielke et al. 2015,  
117 Nehler et al. 2016, Pola et al. 2012, 2014, 2016, Navelot et al. 2019, among others). Only a  
118 few papers quantified clay phases in low temperature environments that constitute upper parts  
119 of geothermal systems (Heap et al., 2017, Heap et al., 2020). To date, only papers addressing  
120 the electrical conductivities of rocks in geothermal systems have quantitatively considered the  
121 impact of clay minerals through empirical relationships, as reported by Ussher et al. (2000)  
122 and Caldwell et al. (1986). This is precisely the aim of this paper, where we investigate the  
123 effect of clay mineral abundances on the porosity, permeability and electrical conductivity of  
124 a series of andesitic samples collected from the caprock formation of the hydrothermal system  
125 of Petite Anse-Diamant (Martinique). Moreover, due to the mutual dependence between the  
126 porous network and petrophysical properties, autoradiographs of rock sections obtained from  
127  $^{14}\text{C}$ -PMMA method will be analysed in parallel with mineralogical maps obtained using  
128 Quantitative Evaluation of Minerals by Scanning electron microscopy (QEMSCAN®) to  
129 identify the development of the porous network with regard to the mineral phases.

## 130 **2. Geological settings**

131 Located in the eastern Caribbean Sea, Martinique Island belongs to the Lesser Antilles  
132 Island arc, which has experienced volcanic activity from the late Oligocene to the present, as  
133 evidenced by the recent and deadly eruptions of Mount Pelée from 1902-1905 and from 1929-  
134 1932. The volcanic activity of the entire island arc results from the subduction of the Atlantic  
135 plate under the Caribbean plate at a rate of 2-4 cm  $\text{y}^{-1}$  (Macdonald 2000). Due to its unique  
136 position, Martinique Island has recorded the most complete history of the island arc leading to  
137 the formation of the following volcanic units, from east to west: the Basal Complex and the

138 Sainte Anne series; the Vauclin Pitault Chain and the South Western Volcanism unit; and the  
139 Morne Jacob, Trois-Ilets, the Carbet Complex, Mount Conil and Mount Pelée, belonging  
140 respectively to the old, intermediate and recent arcs (Figure 1) (Germa 2011). The distribution  
141 from east to west of the erupted rocks is thought to be related to the penetration of an aseismic  
142 ridge under the Caribbean plateau, which led to the flattening of the subducting slab and  
143 therefore shifted the volcanic front towards the west (Bouysse and Westercamp 1990). Thus,  
144 the western part of the island should be the most suitable region for geothermal exploration  
145 due to the potential remnant heat sources allowing the development of geothermal systems.  
146 The first investigations on the geothermal potential of Martinique Island were initiated in the  
147 late 1960s in the Lamentin area where thermal sources have been recognized (Cormy et al.  
148 1970). Several areas were investigated afterwards during exploration campaigns in the 1980s  
149 and 2000s, where the two regions of Mount Pelée and Trois-Ilets showed a strong geothermal  
150 potential, particularly the latter, in the area of Petite Anse located in the southwest of the  
151 island (Figure 1) (Gadalia et al, 2014-2015).

152 In the latter area, geochemical analysis of the local thermal spring Eaux-Ferrée revealed a  
153 reservoir temperature of 190-210°C, according to chemical geothermometers: Na-Li, Ca-K,  
154 Sr-K, Fe-K, 18O(H<sub>2</sub>O-SO<sub>4</sub>) even if the flow rate was low (0.03 l s<sup>-1</sup>), presumably due to the  
155 clayey caprock preventing substantial recharge of the hydrothermal system (Sanjuan et al.  
156 2005; A Gadalia et al. 2014; Coppo et al. 2014). The measured salinity of the latter thermal  
157 spring was 20 g l<sup>-1</sup> (i.e., 2 wt %). This salinity will be used in this article as a reference during  
158 the examination of the electrical conductivities exhibited by the sample series. The dating  
159 work performed by Germa et al. (2011) allowed to constrain the timeline of the island's  
160 volcanic activity and to estimate that the activity in the area of Trois-Ilets occurred between  
161 2.36 Ma and 346 ka ago. At the foot of Morne Jaqueline, where the thermal source of Eaux-  
162 Ferrée is located, evidence of the potential existence of a caprock formation has been revealed



163 by a flank collapse, outcropping andesitic/dacitic rocks affected by argillic alteration with a  
164 montmorillonite-pyrite mineral paragenesis associated with zeolite, sulphate, calcite and iron  
165 oxides (Genter and Roig 2003; Traineau et al. 2013). Other types of fossil hydrothermal  
166 alteration have been recognized in the vicinity of Morne Jacqueline, with notably, a more  
167 acidic alteration represented by kaolinite-alunite mineral associations expressing an advanced  
168 argillic alteration, characteristic of fumarolic activity (White and Hedenquist 1990, Gadalia et  
169 al. 2015). Silica deposits as well as scarce smectite/illite interstratified species have also been  
170 identified that should indicate the circulation of past or present fluid flows originating from  
171 higher reservoir temperatures. Materials and methods

### 172 *3.1 Sampling*

173 On the outcrop located at the foot on the side of Morne Jacqueline, a series of 11 samples  
174 with an andesitic lithology were collected (Figure 1). To obtain an increasing clay abundance  
175 through the whole sample's series, rock samples were collected depending on their apparent  
176 consolidation (poorly consolidated = clay rich) and colour, where a grey facies corresponds to  
177 low-alteration andesite and lighter/yellowish facies corresponds to a higher argillic alteration  
178 progression (Table 1). The detailed petrographic features of the whole sampling is given  
179 below section 4.1.

### 180 *3.2 Quantitative Evaluation of Minerals by Scanning Electron Microscopy (QEMSCAN®* 181 *analysis)*

182 QEMSCAN® is an automatic quantitative analysis system that allows spatially resolved  
183 mineralogical data to be obtained. The system consists of the sequential acquisition of energy  
184 dispersive X-ray (EDX) spectra and back-scattered electron images (BSI) of a polished rock  
185 section. The raw chemical data obtained are then interpreted using a mineralogical database to  
186 associate each measurement point (or pixel) to a mineral. Spatial reconstruction of the

187 interpreted data leads to a mineralogical image of the rock section investigated. In this work,  
188 the mineralogical images as well as the quantitative results acquired from the QEMSCAN®  
189 technique will be used to spatially correlate the mineral phases analysed with the connected  
190 porosity observed from <sup>14</sup>C-PMMA autoradiographs and to study the evolution of  
191 petrophysical properties depending on the mineral phases resulting from hydrothermal  
192 alteration.

193 QEMSCAN® analysis was carried out by the ERAMET Research group on 7 thin  
194 sections (from samples PA 3, PA 4, PA 7.2, PA 10.1, PA 11, PA 12 and PA 13). Chemical  
195 analysis was performed using an FEI Quanta 650 FEG scanning electron microscope mounted  
196 with two energy dispersive spectrometers (EDSs) (Bruker; Synergie 4) and a back-scattered  
197 electron detector (BSE), operating at an acceleration voltage and current intensity of 15 kV  
198 and 5 nA, respectively. The QEMSCAN® software ensured the automatic displacement of the  
199 microscope stage with a step size of 10 µm. The acquisition of the X-ray spectrum for each  
200 measurement point was considered complete for a total count of 2000 photons. The  
201 acquisition time of each thin section was approximately 10 hours. For each area analysed, the  
202 recorded EDS spectrum was attributed to one mineral phase by using the Species  
203 Identification Protocol (SIP) database (Pirrie et al. 2004; Ayling et al. 2012). To supplement  
204 the SIP database results, complementary chemical analysis of the mineral phases was  
205 performed in our laboratory using an SEM JEOL 5600 LV operating with a probe current of 1  
206 nA and an acceleration voltage of 15 kV (detector: SiLi EDS AXS Bruker).

### 207 *3.3 Crystal lattice water abundance (H<sub>2</sub>O<sup>+</sup>)*

208 Clay minerals are known to embed a significant amount of water in the form of  
209 hydroxyls (OH) in their crystal structure. For this reason, the amount of structural water  
210 (H<sub>2</sub>O<sup>+</sup>), generally obtained from bulk-rock chemical analysis, has been used by several  
211 authors as an indicator of the weathering grade of rocks (Jayawardena and Izawa 1994a,

212 1994b; Udagedara et al. 2017). In the present study, bulk measurement of the  $\text{H}_2\text{O}^+$  content is  
213 used to support the clay mineral abundances determined from the mineralogical maps of the  
214 QEMSCAN® system, and furthermore, we use the  $\text{H}_2\text{O}^+$  values as proxies for the clay  
215 mineral abundances of the whole sample series. The bulk-rock chemical analysis was  
216 conducted at the SARM laboratory of Nancy (CRPG, France) on 1 g of each sample,  
217 previously ground to reach an average size between 80  $\mu\text{m}$  and 1 mm. The powder samples  
218 were heated at 105°C to remove the free and adsorbed water and then placed in an oven at  
219 1000°C under a nitrogen atmosphere for determination of the  $\text{H}_2\text{O}^+$  abundance, following the  
220 Karl Fisher titration protocol.

### 221 *3.4 Methylene blue*

222 Cost-effective and easy to implement, the methylene blue (MB) method can be used  
223 during the exploration step of a geothermal project to rapidly evaluate the abundance of  
224 smectite minerals on a semi-quantitative basis. The MB method is commonly applied in civil  
225 engineering, to estimate the clay content of soils, or to determine the cation exchange capacity  
226 (CEC) of clay minerals (Hang and Brindley 1970; Kahr and Madsen 1995; Lorenz 1999;  
227 Yukselen and Kaya 2008). MB is an organic dye with the corresponding chemical formula of  
228  $\text{C}_{16}\text{H}_{18}\text{ClN}_3\text{S}$ , which is positively charged when dissolved in water ( $\text{C}_{16}\text{H}_{18}\text{N}_3\text{S}^+$ ). Therefore,  
229 when the organic dye is added to a suspension containing clay minerals, the cationic dye can  
230 be adsorbed onto the negatively charged surfaces as well as onto the interlayer surfaces of the  
231 clay minerals. The MB test was conducted by preparing a suspension of 30  $\text{cm}^3$  using 2 g of  
232 powder with a grain size of  $<50 \mu\text{m}$ . The suspensions were stirred overnight to ensure  
233 disintegration of any remaining aggregates. The spot test was performed following the  
234 methodology of Santamarina et al. (2002), which consists of adding a methylene blue solution  
235 to the sample suspension in increments of 0.5 mL and waiting for 1 min between each MB  
236 addition. After 1 min, a drop of the suspension is placed on paper filter to evaluate if all MB

237 molecules have been adsorbed. When MB molecules are in excess (i.e., all adsorption sites  
 238 are occupied), a blue halo is formed around the aggregate. The MB value is then calculated  
 239 from the volume of the MB solution used,  $V_{MB\ sol}$ , and the mass of the sample (Equation (1)):

$$240 \quad MB = \frac{m_{sample}}{V_{MB-sol}} \quad (1)$$

### 241 *3.5 Bulk Connected Porosity*

242 The bulk connected porosity of the samples was evaluated following the triple weight  
 243 method (TW) (Franklin et al. 1981). The method consists of the measurement of three  
 244 different weights, depending on the state of the sample: dry, water-saturated and water-  
 245 saturated suspended in water. Rock pieces of  $\sim 10\text{ cm}^3$  were partially immersed in purified  
 246 water under vacuum for imbibition. This volume was considered as sufficient in consideration  
 247 of the representative elementary volume needed for the grain or mineral size distribution of  
 248 the samples. Any potential fluid excesses present on the sample's surface were removed using  
 249 a wet paper before measurement of the sample's weight in the saturated state. The saturated  
 250 samples were dried for 48 h in an oven at  $105^\circ\text{C}$  to determine the dried sample weight. The  
 251 sample bulk volume  $V_s$  is calculated using Archimedes' principle by Equation (2):

$$252 \quad V_s = \frac{w_w - w_a}{\rho_w} \quad (2)$$

253  $w_w$  is weight of water-saturated sample measured at ambient air.  $w_a$  is weight of water-  
 254 saturated sample plunged in water.  $\rho_w$  is the mass unit weight of water.

255 The pore volume  $V_p$  is calculated with Equation (3):

$$256 \quad V_p = \frac{w_w - w_d}{\rho_w} \quad (3)$$

257 where  $w_d$  is the weight of the dried sample.

258 Finally, the connected porosity  $\phi_{tw}$  is calculated from Equations (2) and (3):

$$259 \quad \phi_{tw} = \frac{V_p}{V_s} = \frac{w_w - w_d}{w_w - w_a} \quad (4)$$

260 Here, it was assumed that the swelling of expandable clay minerals resulting from the  
261 complete water saturation of samples did not significantly influence porosity measurement.

### 262 *3.6 Connected porosity from the $^{14}\text{C}$ -PMMA method*

263 Bulk measurements of properties such as the electrical conductivity and permeability  
264 are intimately linked to the characteristics exhibited by the porous network of rocks (e.g.,  
265 connectivity, pore type, pore size distribution, anisotropy and tortuosity) (Avellaneda and  
266 Torquato 1991; Milsch et al. 2008; Wright et al. 2009). In this section, connected porosity  
267 maps of the samples obtained by the  $^{14}\text{C}$ -PMMA technique are analysed: (1) to characterize  
268 the type of porosity involved in the samples and (2) to analyse the porosity distribution with  
269 regard to the mineral phases identified in the QEMSCAN® analysis.

270 Quantification and imaging of the connected porosity of the samples were performed  
271 using the  $^{14}\text{C}$ -PMMA methodology developed in the 1990s (Hellmuth and Siitari-Kauppi  
272 1990; (Hellmuth et al. 1993; Siitari-Kauppi 2002). The method consists of measuring the  
273 radiation arising from samples saturated beforehand with a  $^{14}\text{C}$ -labelled tracer. Polished rock  
274 sections of impregnated samples are put into contact with an autoradiographic film (FA)  
275 composed of an emulsion of silver bromide crystals (AgBr) of which the  $\text{Ag}^+$  cations can be  
276 reduced to metallic silver by absorption of the electrons arising from the  $^{14}\text{C}$ -labelled tracer.  
277 The latter process results in a blackening of the autoradiographic film corresponding to the  
278 distribution of the radionuclide tracer and therefore the connected porosity. After exposure,  
279 the autoradiographic film is developed and digitized for image analysis. In this study, core  
280 samples with dimensions of 4 cm in diameter and 3 cm in height were dried in an oven at  
281  $40^\circ\text{C}$  for one month and placed under vacuum for three hours to remove any residual water.  
282 Impregnation of the samples with a  $^{14}\text{C}$ -MMA solution of an activity of  $178\text{ kBq mL}^{-1}$  was  
283 performed under vacuum for one month at the Laboratory of Radiochemistry (Helsinki,  
284 Finland). Polymerization of the  $^{14}\text{C}$ -MMA solution in the porous network was ensured by

285 heating the sample in a bath at 55°C for 16 hours. Finally, the impregnated samples were  
286 sawed and polished to ensure the optimal contact between the autoradiographic film and the  
287 rock sections. The autoradiographic films used in this work were KODAK BioMax MR films  
288 (resolution: 20 µm) for a total exposure time of ~4 days. Digitization of the autoradiographic  
289 film into grey-level 16-bit depth images was performed using a Microtek Artix Scan F1  
290 scanner with a resolution of 2400 dpi (pixel size: 10.6 µm). Due to the non-linear response of  
291 the autoradiographic film to irradiation, 14 standards of pure <sup>14</sup>C-PMMA with known  
292 activities were exposed at the same time to provide an empirical relationship between the  
293 blackening of the film and the connected porosity. However, the maximal range of electrons  
294 emitted by the <sup>14</sup>C in PMMA has been estimated by Kanaya and Okayama (1972) at ~224  
295 µm, which is significantly higher than the thickness of the thin sections used for the  
296 acquisition of the autoradiographs (~30 µm). Following this condition and since the thickness  
297 of the <sup>14</sup>C-PMMA plugs used as standards for the calibration have a thickness on the order of  
298 a few millimetres, the porosities calculated from the calibration process are underestimated.  
299 Table 2 provides an overview of comparison of <sup>14</sup>C-PMMA porosity method with more  
300 popular imaging methods, such as Scanning Electron Microscope (SEM) and X-Ray  
301 Computed Microtomography (XRCT). Other class of methods provide pore size distribution  
302 (Hg-porosimetry and adsorption methods), or provide merely bulk porosity value (TW  
303 method and He-pycnometry). The main advantage of <sup>14</sup>C-PMMA method consists on his  
304 ability to provide quantitative porosity maps which are easy to analyse, and which account all  
305 connected pores of the studied section, regardless of pore size (it is why this method is  
306 sometimes called multi-scale). For instance, concerning microcracks, the method is able to  
307 map at core scale all cracks, whatever their aperture (Mazurier et al., 2016; Bonnet et al.,  
308 2020). This is not the case for XRCT or SEM, which does not provide porosity maps, but  
309 where pore can be detected by image segmentation. The smaller pores are not detected using

310 these methods because their size are smaller than pixel or voxel size. In fact, for these  
311 conventional imaging methods, the resolution is a function of the sample size, controlling the  
312 pixel or voxel size. <sup>14</sup>C-PMMA has his own drawbacks, such as the need to manipulate open  
313 radioactive sources, and the fact that it is not 3D (Table 2). However, the cost remains the  
314 same than XRCT, and the total analysis time is also quite comparable to other porosimetric  
315 methods. As emphasized by Table 2, the bulk methods have not to be ignored, because they  
316 provided reference values for porosity calculation.

### 317 *3.7 Intrinsic Water Permeability*

318 We used here the same device employed by Sardini et al. (1996), except that core  
319 samples with a diameter of 35 mm were covered on their side with LOCTITE EA 9483 epoxy  
320 resin to avoid any lateral leakage of water during the permeability experiment. The high  
321 viscosity of this epoxy resin prevents intrusion in the pore space of the samples. The  
322 thicknesses of the core samples range from 10 to 15 mm. The sample thicknesses were large  
323 compared to rock grain size in order to have a measurement representative of the whole rock.  
324 Large phenocrysts of feldspars or hornblende can be however the same size as the sample  
325 thickness used for these measurements. It was not possible to use thicker samples because the  
326 maximal thickness acceptable by the used device is 2.5 cm. Figure 2 shows the experimental  
327 setup for the permeability measurement.

328 Permeability experiments were performed in steady state flow conditions, using a  
329 pressure gradient ( $\Delta P$ ) kept between 1 and 2 bar across the samples. Two nitrogen reservoirs  
330 imposed the up and downstream pressure into the H<sub>2</sub>O vessel (Figure 2). These reservoirs  
331 were isolated from the water circuit by an impervious membrane; the pressures imposed by  
332 the inflation of these N<sub>2</sub> reservoirs provided the pressure gradient necessary to the flow of  
333 water through the rock sample. The differential pressure was recorded during the experiment,  
334 and the flow rate of water was measured using a capillary (Figure 2). The experimental flow

335 rate being very low (ranged between 0.7 to  $4 \times 10^{-4}$  mm<sup>3</sup>/s), the permeability was calculated  
336 assuming a laminar flow regime, using Darcy's law:

$$337 \quad k = \frac{Q\eta l}{S \Delta P} \quad (5)$$

338 where  $k$  is the intrinsic permeability (m<sup>2</sup>),  $Q$  is the measured flow rate (m<sup>3</sup> s<sup>-1</sup>),  $\eta$  is the  
339 dynamic viscosity (Pa.s),  $S$  is the surface area of the plug sample corrected from the  
340 impregnation resin (surface efficient for the water flux) ( $7.07 \cdot 10^{-4}$  m<sup>2</sup>) and  $l$  is the length of  
341 the core sample.

342

### 343 *3.8 Electrical conductivity*

344 Electrical measurements were performed with a Solartron Impedance Analyser 1260  
345 using 6 NaCl brines with increasing salinity levels of 0.01; 0.05; 0.1; 0.5; 1 and 2 wt %. Note  
346 that the range of salinities used encompasses the range of total salt concentrations commonly  
347 found for geothermal fluids (0.1 – 1 wt %) (Henley and Ellis 1983). Sample saturation was  
348 performed at 20°C by immersion in NaCl brines for two weeks.

349 A resistivity cell of Teflon was designed to receive the plug samples used for the  
350 permeability measurements (Figure 3). After placing the plug sample in the resistivity cell,  
351 NaCl brine was added through the two upper apertures of the cell to ensure electrical  
352 conduction between the electrodes and the surface of the plug sample. Acquisition of the  
353 impedance spectra was performed with the two-electrode configuration in the 0.1 -  $3 \cdot 10^6$  Hz  
354 frequency range. The conductivity magnitude  $|\sigma|$  was obtained with following Equation (6):

$$355 \quad |\sigma| = \frac{1}{|Z|} \frac{l}{s} \quad (6)$$

356 where the impedance amplitude  $|Z|$  has been selected at a frequency close to 1 kHz (e.g., Lévy  
357 et al., 2018) for which the imaginary part of the complex impedance  $Z$  was minimum. For



358 simplicity in writing, the conductivity magnitude,  $|\sigma|$ , will be simply named the electrical  
359 conductivity,  $\sigma$ , hereafter.

## 360 **4. Results and discussion**

### 361 *4.1 Progression of hydrothermal alteration*

362 The hydrothermal alteration exhibited by the sample series has already been discussed  
363 thoroughly in a previous article (Delayre 2018). In this article, we report the main results and  
364 petrographic features of the samples that we believe play a significant role in the evolution of  
365 the petrophysical properties investigated.

366 Figure 4 presents selected areas of the mineral maps obtained in the QEMSCAN®  
367 analysis of samples PA 13 and PA 4 and PA 7.2, PA 10.1, PA 12 and PA 11. For the whole  
368 sample series, the mineral phases identified in the QEMSCAN® analysis consist of feldspar  
369 minerals belonging to the plagioclase series (andesine, labradorite, oligoclase and bytownite),  
370 hornblende and quartz, corresponding to primary minerals, while alteration paragenesis is  
371 represented by clay minerals (montmorillonite and kaolinite), iron oxides, carbonates and  
372 sulphide minerals. The matrix of the rock with the above-mentioned primary minerals  
373 embedded corresponds to a mesostasis where feldspar microlites and devitrification of glass  
374 have been observed using optical microscopy in a previous work (Delayre 2018). The  
375 alteration paragenesis exhibited by the samples is very common in hydrothermally altered  
376 volcanic rocks and can be identified as argillic alteration (White and Hedenquist 1990;  
377 Pirajno 2009). From a more petrographic point of view, the size of the feldspar and  
378 hornblende crystals ranges from the sub-millimetre to the millimetre and frequently exhibit  
379 rectangular and sub-hexagonal sections, respectively (Figure 4). The lowest alteration  
380 intensity is observed in sample PA13, which has been discriminated as two different samples,  
381 PA13.1 and PA13.2, where the latter corresponds to the wall-rock area of small fractures

382 characterized by higher abundances of silica and iron oxides, as observed during field  
383 sampling (arrows 1 and 2, respectively, sample PA13.2 in Figure 4). Crystallization of  
384 montmorillonite produces a patchy alteration pattern in the mesostase along with a moderate  
385 alteration of hornblende crystals, as shown in the PA 13.1 sample (arrow 3, Figure 4).  
386 Intragranular alteration of hornblende crystals is clear in the PA 4 sample, where  
387 montmorillonite crystallizes in association with the iron oxide phases along hornblende  
388 cleavages intersecting at 120° (Figure 4). Among the samples investigated, a particular feature  
389 is found for PA7.2, where a vein of predominantly montmorillonite is observed and crosses  
390 the entire sample (Annex 1). In Figure 4, the PA10.1 sample exhibits a higher alteration  
391 intensity revealed by the stronger pervasiveness of alteration of montmorillonite and silica  
392 present throughout the mesostase and hornblende crystals, which, for this sample, are  
393 completely replaced by montmorillonite and sulphide minerals ( $\pm$  silica  $\pm$  iron oxides)  
394 (arrows 1 and 2, respectively; Figure 4). The strong association of montmorillonite and  
395 sulphide minerals is not systematic throughout the sample series investigated and should  
396 reveal either a chemical variation in fluid composition affecting the rocks or local variation in  
397 the pre-existing lithology. Such variation in fluid composition is supported by the  
398 crystallization of carbonates, with calcite as the major mineral phase, manifested as infilling  
399 of fractures and dissolution vugs in sample PA10.1.

400 Strong pervasive alteration is observed in the PA 12 sample, where at this stage,  
401 complete replacement of the hornblende crystals by montmorillonite, strongly associated with  
402 iron oxides, is observed (arrow 1, PA 12, Figure 4). Dissolution of the mesostase as well as of  
403 feldspar minerals is revealed by the increased number of white pixels corresponding to  
404 porosity in the mineral maps obtained in the QEMSCAN® analysis. At this stage, only quartz  
405 crystals remain unaffected by hydrothermal alteration.

406 With regard to the alteration intensity, the end member of this sample series is represented by  
407 PA 11, where intense pervasive alteration is observed (Figure 4). In addition to the total  
408 replacement of the hornblende crystals by montmorillonite and silica ( $\pm$  kaolinite) (arrow 3,  
409 PA 11, Figure 4), the PA 11 sample presents frequently open cavities resulting from the  
410 quasi-total dissolution of feldspar crystals in which few remnants can still be observed (arrow  
411 2, PA 11, Figure 4). This dissolution vugs are often completely or partially filled with  
412 kaolinite and silica and to a lesser extent with montmorillonite (arrow 1, PA 11, Figure 4). In  
413 this last sample, such a strong occurrence of kaolinite could be attributed to advanced argillic  
414 alteration resulting from the circulation of more acidic (low pH) fluids. However, the absence  
415 of minerals such as alunite, typical of advanced argillic alteration, and the low crystallinity of  
416 kaolinite revealed by X-ray diffraction (XRD) analysis could indicate a weathering origin  
417 (Hughes, 1980; White and Hedenquist, 1990; Delayre, 2018).

#### 418 *4.2 Quantitative evaluation of hydrothermal alteration*

419 The quantitative results obtained in the QEMSCAN® analysis are presented in Table 3, in  
420 which samples were ranked from left to right with increasing clay mineral abundances.  
421 Overall, good agreement is found between the quantitative results and the qualitative  
422 characterization performed in the previous section. The abundance of feldspar minerals is  
423 relatively stable throughout the sample series, varying between 30 and 40 %, except for the  
424 PA12 and PA11 samples, which display abundances of 23.31 and 4.27 %, respectively, due to  
425 the partial or total dissolution of feldspar crystals. Feldspars are the main source of alumina  
426 for montmorillonite and kaolinite. This explain their decreasing amount as the alteration  
427 degree increases. This replacement is confirmed by the shape of montmorillonite aggregates  
428 as observed in PA11 (rectangular sections in Figure 4).The raw quantitative results do not  
429 seem to reflect the replacement or dissolution of the mesostase. However, a general

430 decreasing trend is found when abundance recalculation is performed considering the white  
431 pixels in the mineral maps.

432 As observed in the mineral maps, only the PA 13.2 sample, the least argillized of the sample  
433 series, shows a high abundance (13.9 %) of hornblende, where due to the higher alteration  
434 intensity, this value falls below 1 %. Nevertheless, no significant trend of hornblende  
435 abundance can be found with increasing amounts of clay mineral phases, as depicted by the  
436 PA10.1 sample exhibiting a hornblende abundance of 0.1 %, considered moderately  
437 argillized. The abundances of carbonates and iron oxides are low (i.e., < 3 %) and erratic  
438 throughout the sample series even though PA13.2 presents a slightly higher iron oxide  
439 abundance. With regard to the major hydrothermal alteration products, both kaolinite and  
440 montmorillonite are ubiquitous in all samples, where for the latter, an increasing trend from  
441 4.69 to 22.74 % is observed. For the former, the abundances are systematically below 1 %,  
442 with the exception of samples PA 12 and PA 11, which display abundances of 3.92 and 14.82  
443 %, respectively.

444 As mentioned in the materials and methods section in this study, only certain samples  
445 of the whole series were selected for QEMSCAN® analysis. Thus, to include the remaining  
446 samples in the petrophysical analysis, the abundance of structural water in each sample was  
447 determined in view of using its value as a proxy for the clay mineral abundance. The results  
448 are presented in Table 4 and Figure 5, where the total clay mineral abundances are plotted  
449 against the  $H_2O^+$  values obtained from the bulk-rock chemical analysis.

450 A good and linear correlation is found ( $R^2= 0.9854$ ) between the total clay mineral  
451 abundances and crystal lattice water proportions, which therefore confirms the assumption  
452 established previously. However, such indicators should be handled carefully when used for  
453 the semi-quantitative evaluation of clay minerals. Indeed, several hydrothermal minerals (e.g.,

454 the zeolite group, alunite, epidote, pyrophyllite) can also exhibit embedded water in their  
455 crystalline structures and therefore may bias the results if used without caution.

#### 456 *4.3 Comparison of the mineral maps and autoradiographs from the <sup>14</sup>C-PMMA method*

457 Figure 6 presents the mineral maps of the PA13, PA4, PA10.1, PA12 and PA11 samples  
458 in parallel with autoradiographs of the same areas. Notably, several fractures undetected by  
459 microscopy are clearly revealed by the autoradiographs of samples PA13, PA4 and PA10.1.  
460 For the first two samples, PA12 and PA14, no significant infilling or evidence of fluid-rock  
461 interactions in the vicinity of the microfractures was observed in the mineral maps. This could  
462 indicate that the generation of the observed microfractures was posterior to hydrothermal  
463 alteration. Conversely, deposition of iron oxides as well as carbonates was observed in the  
464 main fracture and in the dissolution vugs. The PA10.1 sample revealed that these structures  
465 were used as pathways for hydrothermal fluid circulation. In the autoradiographs, such  
466 crystallization of carbonates is associated with low porosity areas, as observed in the PA10.1  
467 and PA12 samples (arrow 3 and arrow 2 in Figure 6). Additionally, deposition of silica (and  
468 presumably of iron oxides) tends to have a similar impact by clogging the connected pores  
469 and therefore reducing the overall average porosity of the rock. This process is particularly  
470 notable for the PA13 sample, where, in the autoradiographs, a large porosity contrast is found  
471 between PA13.1 and PA13.2, displaying silica abundances of 4.91 and 8.64 %, respectively  
472 (Table 3). The sulphide minerals are also congruent with the low porosity areas when infilling  
473 dissolution vugs or in pseudomorphosed hornblende crystals (arrow 1, PA10.1, Figure 6).

474 Overall, an increasing trend of the connected porosity is found for the whole sample series  
475 when calculated from the autoradiographs (Table 4), although underestimated, as explained in  
476 section 3.6. In the autoradiographs presented, the porous areas are associated mainly with the  
477 clay mineral phases, dissolution vugs and fractures and are visible as dark areas in the  
478 autoradiograph. Notably, montmorillonite crystallizing along hornblende cleavages is

479 associated with porous areas (darker) as clearly revealed by the autoradiograph of the PA 4  
480 sample (arrow 1, Figure 6). Destabilization of the mesostase through dissolution and  
481 replacement by mineral paragenesis leads to a global porosity increase of the rock matrix  
482 where even the pseudomorphosed hornblende crystals are difficult to discriminate from the  
483 rock matrix (arrows 3 and 1 for PA12 and PA11, respectively, Figure 6). Conversely, the  
484 dissolution vugs associated with feldspar crystals in PA11 are clearly distinguished from the  
485 rock matrix (arrow 2, PA 11, Figure 6). Infilling of kaolinite, observed in the same feldspar  
486 crystal, seems to reduce the porosity. Only quartz crystals remain unaffected by hydrothermal  
487 alteration and can be easily observed due to their lower porosity (arrow 3, PA11, Figure 6).

#### 488 *4.4 Evolution of the bulk connected porosity and intrinsic permeability*

489 Figure 7 (A) presents the evolution of the connected porosity estimated from the triple  
490 weight method as a function of the structural water proportion ( $H_2O^+$ ), used in this study as a  
491 proxy of the clay mineral abundance. The connected porosities of the samples range from  
492 3.74 to 35.35 % and show strong linear relationships with the  $H_2O^+$  values ( $R^2= 0.8835$ ),  
493 revealing that in the rock series investigated, the dominant process of porosity creation is  
494 related to the crystallization of clay minerals (i.e., montmorillonite and kaolinite). Moreover,  
495 the silicification and crystallization of iron oxides reported above for sample PA13.2  
496 compared to PA13.1 seems to have a great impact on the connected porosity, inducing a  
497 decrease from 10.5 to 4.48 %. The moderate scattering of porosity data at low  $H_2O^+$  values is  
498 attributed to the presence of fractures and dissolution vugs causing an increase in connected  
499 porosity, as observed for the PA10.1 sample.

500 The intrinsic permeabilities measured for the sample series, ranging from  $7.7 \cdot 10^{-20}$  to  
501  $5.4 \cdot 10^{-17} \text{ m}^2$ , show an increasing trend with the connected porosities measured by the TW  
502 method (Figure 7, B). The highest permeability value is found for the PA11 sample and seems  
503 unexpected since this sample is the most argillized among the samples in the present series.

504 This finding should be related to the strong destabilization of the rock matrix as well as to the  
505 dissolution vugs developed at the expense of the feldspars, as observed in the mineral maps  
506 and autoradiographs. Numerous data of permeability reported in the literature for effusive  
507 andesites (Wright et al., 2009, Farquharson et al, 2015, Mielke et al, 2015, Heap and  
508 Kennedy, 2016, Heap et al., 2018, Mordensky et al, 2018 among others) exhibit a range of  
509 permeability from  $10^{-17}$  to  $10^{-11}$  m<sup>2</sup>. Nevertheless lower values down to  $10^{-19}$ - $10^{-20}$ m<sup>2</sup> are also  
510 mentioned (Wollentz and Heiken, 1992; Petrov et al, 2005; Navelot et al, 2018). It should be  
511 noted that most of the values reported in the literature are gas permeabilities. Other data can  
512 be found in the literature on lavas or lavas block of various compositions (Bernard et al., 2007  
513 ; Dobson et al, 2003; De Maisonneuve et al, 2009 ; among others) or on pyroclastic materials  
514 (Degruyter et al., 2010 ; Heap et al., 2017 ; Heap et al., 2020). The permeability data reported  
515 in the literature are 2 to 4 orders of magnitude higher than the permeabilities measured in this  
516 work. Part of this shift could be explained by the fact that permeability values found in the  
517 literature are mainly gas permeability while in the present study we determined water  
518 permeability. This latter value is probably closer to real permeability in natural systems  
519 affected by smectitic alteration. Indeed smectitic material consists in expandable clay phases  
520 which can strongly affect the permeability in water saturated conditions. As an illustration in  
521 Krafla system, Escobedo (2018) observed 2-3 orders of magnitude between gas and water  
522 permeabilities in hyaloclastic formations affected by smectitic alteration. From this  
523 observation, we deduce that hydrothermal alteration induces a consequent decrease in the  
524 permeability (at least one order of magnitude) due to the formation of expandable clay  
525 minerals. The subsequent dissolution of the rock matrix and pre-existing minerals, however,  
526 counteracts this process by opening new pathways for fluid circulation, thereby enhancing  
527 permeability. Intermediate clay-rich facies that would complete the data set between PA10.1  
528 and PA11 would be needed to increase the robustness of the relationship observed.

529 Unfortunately, such samples were not recognized at the investigated scale due to the  
530 sharpness of the transition between very altered to poorly altered zones.

#### 531 *4.5 Impact of argillic alteration on the electrical conductivity*

532 Figure 8 shows the variation in bulk conductivity measured for each sample depending  
533 on the electrical conductivity of the saturating fluid on a log-log scale. For all samples, the  
534 bulk conductivity increases with increasing electrical conductivity and presents the typical  
535 evolution observed for argillized rocks containing clay minerals with a significant cation  
536 exchange capacity (CEC) (Revil et al. 2002; Flóvenz et al. 2005; Komori et al. 2010). Indeed,  
537 the electrical conduction in saturated rocks typically involves two different mechanisms:  
538 electrolytic conduction, related to the migration of cations and anions through the connected  
539 pore space, and surface conduction, enabled by the presence of high-CEC minerals (e.g.,  
540 smectite), present at the surface as weakly adsorbed cations. The latter mechanism is  
541 generally justified through the formation of an electrical double layer at the mineral surface  
542 when put in contact with an electrolyte (Gouy 1910; Chapman 1913 and Stern 1924). Both  
543 mechanisms are represented in Figure 8. At a low solution conductivity (from 200 to ~2000  
544  $\mu\text{S cm}^{-1}$ ), surface conduction is the dominant electrical conduction mechanism and results in  
545 the apparent flat part of the plot, especially notable for the PA 12 sample, while at a higher  
546 solution conductivity (from ~10,000 to 30,000  $\mu\text{S cm}^{-1}$ ), electrolytic conduction dominates,  
547 resulting in the linear increasing trend (log-log scale) observed.

548 As expected, the two most argillized samples (i.e., PA12 and PA11) have significantly  
549 higher bulk electrical conductivities than the rest of the samples due to the higher abundances  
550 of montmorillonite. However, the PA 10.1 sample, which was considered to be moderately  
551 argillized (clay mineral abundance: 8.09 %), exhibited an excess electrical conductivity. From  
552 the QEMSCAN® analysis, a strong association of montmorillonite with sulphide minerals  
553 was observed, unique among the samples investigated. If these sulphide minerals constitute a



554 connected network, they could be the reason for the high electrical conductivity. A third  
555 mechanism of electrical conduction could therefore be involved in the PA 10.1 sample  
556 corresponding to electronic conduction, in which the charge carriers are the valence electrons  
557 located in the outer shell of metallic atoms.

558 In the area of Petite-Anse, the magnetotelluric survey performed during the 2012-2013  
559 exploration phase by Coppo et al. (2014) revealed electrical resistivities  $< 10$  Ohm.m at  
560 shallow depths. This value is very similar to the electrical resistivities measured in this work  
561 for the most argillized samples PA11 and PA12 exhibiting resistivities (after conversion from  
562 conductivities) ranging from 9.6 to 1.8 Ohm.m and from 8.0 to 2.7 Ohm.m, respectively,  
563 which are in the range of the saturating solution salinities used.

564 In Figure 9 (A), the bulk conductivities of the samples saturated with the 2 wt % NaCl  
565 solution are plotted against the structural water proportions and methylene blue values (A and  
566 B, respectively). An increasing trend is observed between the bulk conductivities and  
567 structural water proportions with a relatively good correlation ( $R^2= 0.8591$ ), as expected from  
568 the increasing contribution of the surface conductivity resulting from the increasing  
569 montmorillonite abundances. From this figure, it seems nevertheless difficult to discriminate  
570 the samples with low  $H_2O^+$  values (low clay mineral abundances). A better correlation  
571 coefficient is found ( $R^2= 0.9579$ ) when the electrical conductivities are plotted against the  
572 methylene blue values (Figure 9, B). This results from the fact that the methylene blue value  
573 is mainly representative of the clay mineral abundance with a high CEC. On the other hand,  
574 structural water proportion measurement integrates the kaolinite abundance, a clay mineral  
575 known to have a low CEC and therefore contributes to a limited extent to electrical  
576 conduction, hence the lower correlation coefficient.

577 Several indicators have been used in the literature to evaluate the contribution of the  
578 surface conductivity arising from clay minerals, especially smectite. The surface or interface

579 conductivity is generally derived from electrical conductivity models, such as the one of  
580 Waxman and Smits (1968) or more recently, the one of Revil and Glover (1998). In this work,  
581 to evaluate the contribution of surface conductivity, we used the isoconductivity point, as  
582 defined by Shainberg et al. (1980) corresponding to the conductivity value for each sample  
583 where its bulk conductivity and solution conductivity are equal.

584 Figure 10 presents the plot of this indicator against the methylene blue value. As shown in  
585 Figure 13, we were able to determine the isoconductivity point only for 5 samples (i.e., PA  
586 3.2, PA 5.1 PA 10.1 PA 12 and PA 11) due to the low bulk conductivities of the remaining  
587 samples. A strong and linear correlation is found ( $R^2= 0.9806$ ) between the isoconductivity  
588 point and methylene blue value, revealing the strong relation between this indicator and the  
589 abundance of montmorillonite.

## 590 **5. Conclusion**

591 In this work, the evolution of the petrophysical properties (i.e., connected porosity,  
592 permeability and electrical conductivity) of the samples collected at the Petite Anse-Diamant  
593 hydrothermal system was investigated on the basis of the quantitative evaluation of minerals  
594 by scanning electron microscopy (QEMSCAN®) method. The crystal lattice water abundance  
595 was found to be a relevant indicator of the clay mineral abundance for the sample series.  
596 From the  $^{14}\text{C}$ -PMMA autoradiograph analysis, the development of argillic alteration,  
597 sometimes superimposed by weathering alteration (i.e., PA 11), leads to an increase in the  
598 connected porosity, primarily due to the replacement of the rock matrix and pre-existing  
599 minerals by clay minerals, identified here as montmorillonite and kaolinite. Dissolution vugs  
600 and fracturing were found to be significant in several samples and contribute to the increases  
601 in connected porosities observed. The crystallization of silica, iron oxides and carbonates  
602 counteracts this process, leading to a decrease in the connected porosity. The permeability  
603 measurements revealed a significant decrease of 2 to 4 orders of magnitude when compared to

604 the permeability data acquired for andesites in the literature. No clear relation to the increase  
605 in clay mineral abundance was observed; however, the low permeabilities classically  
606 observed for rocks belonging to the caprock formation should be reached during the first steps  
607 of argillic alteration development. The electrical conductivity measured for the whole sample  
608 series shows a linear relationship with the montmorillonite abundance, represented in this  
609 work by the methylene blue value, which is easy to acquire in the laboratory and in the field.

610         Consequently, these new data obtained by coupling different techniques provide three  
611 results in a practical and modeling viewpoint. First, they confirm the interest of using  
612 geophysical methods based on resistivity measurement (e.g., Direct Current resistivity method  
613 and low-frequency electromagnetic methods) to locate caprock formations especially rich in  
614 montmorillonite. Let us recall that these geophysical techniques referred as electrical methods  
615 share the advantages of being fast, non-intrusive and covering wide areas of investigation in  
616 comparison with conventional methods (e.g., drilling, field sampling). Second, our data show  
617 that there exist no clear relationship between permeability and clay abundance and thus  
618 between permeability and electrical resistivity. Consequently, there is little hope to  
619 characterize quantitatively in the field the hydraulic properties of caprock formations by  
620 electrical methods. Third, the combination of mineral maps and spatial distribution of the  
621 connected porosity observed in autoradiographs allows to clearly discriminate two types of  
622 porosity existing in caprock formations: porosity associated with clay mineral phases and that  
623 related to dissolution vugs and fractures. Thus our approach provides a quantitative  
624 petrographical basis for modeling the hydraulic properties of caprock formations considered  
625 as dual-porosity systems.

626         This work suggests the need for further investigations in two directions. First, this  
627 work has accounted for classical petrophysical properties (bulk connected porosity,  
628 permeability and electrical conductivity), but recent studies carried out in similar contexts

629 have shown the possibility of using new non-intrusive indicators based on low-frequency  
630 electromagnetic measurements (e.g., the quadrature conductivity and the normalized  
631 chargeability; see Revil et al., 2017; Ghorbani et al., 2018; Lévy et al., 2019). These new  
632 indicators can be useful in supplementing the information provided by conventional electrical  
633 resistivity measurements and should also be compared to mineralogical and petrographic data.  
634 Second, the methodology used in this work based on the coupling of innovative techniques  
635 (mineral mapping, <sup>14</sup>C-PMMA method and petrophysical properties) could be applied to  
636 investigate the impact of HT hydrothermal alteration (200-300°C) located at the reservoir  
637 level of high-enthalpy hydrothermal systems. These studies would clearly require an  
638 adaptation of the experimental conditions through measurement of the same properties as a  
639 function of the temperature and pressure.

640

641 **Acknowledgements:** The authors are grateful to Juuso Sammaljärvi, Eveliina Muuri and  
642 Marja Siitari-Kauppi for the fruitful discussions on the <sup>14</sup>C-PMMA method and for the  
643 preparation of the samples. This work was partly carried out with the financial support of the  
644 ANR Agence Nationale de la Recherche (French National Research Agency), project ANR-  
645 17-CE06-0012-03 ExCiTING (Exploration des ressources géologiques et des réservoirs par  
646 prospection géophysique des propriétés des argiles). The authors also acknowledge financial  
647 support from the European Union (ERDF) and Région Nouvelle Aquitaine. We would like to  
648 thank Kristian Bär and Jamie Farquharson for their thorough review which helped us improve  
649 the manuscript.

650

651 Appendix A. Supplementary data. QEMSCAN® maps.

652

653 **References**

654 Ahmed, A. S., Revil, A., Byrdina, S., Coperey, A., Gailler, L., Grobbe, N., Viveiros F., Silva  
655 C., Jougnot D., Ghorbani A., Hogg, C., Kiyani D., Rath V., Heap M.J., Grandis H.,  
656 Humaida H., 2018. 3D electrical conductivity tomography of volcanoes. *J. of Volcanol.*  
657 *Geotherm. Res.* 356, 243-263.

658 Archie, G.E., 1942. The electrical resistivity log as an aid in determining some reservoir  
659 characteristics. *Transactions of the AIME* 146 (01): 54–62.

660 Arnason, K., Karlsdottir, R., Eysteinnsson, H., Flóvenz, O.G., Gudlaugsson, S.T., 1992. The  
661 resistivity structure of high-temperature geothermal systems in Iceland. In: E. Iglesias, D.  
662 Blackwell, T. Hunt, J. Lund and S. Tamanyu (Eds.), *Proceedings of the World Geothermal*  
663 *Congress 2000, Kyushu-Tohoku, Japan*, 923–28.

664 Avellaneda, M. Torquato, S., 1991. Rigorous link between fluid permeability, electrical  
665 conductivity, and relaxation times for transport in porous media. *Physics of Fluids A: Fluid*  
666 *Dynamics* 3 (11): 2529–40.

667 Ayling, B., Rose, P., Petty, S., Zemach, E., Drakos, P., 2012. QEMSCAN (Quantitative  
668 Evaluation of Minerals by Scanning Electron Microscopy): Capability and application to  
669 fracture characterization in geothermal systems. *Proceedings of the Thirty-Seventh*  
670 *Workshop on Geothermal Reservoir Engineering*. Stanford, California: Stanford  
671 University, January 30 - February 1, 2012.

672 Beaufort, D., Patrier, P., Meunier, A. Ottaviani M.M., 1992. Chemical variations in  
673 assemblages including epidote and/or chlorite in the fossil hydrothermal system of Saint  
674 Martin (Lesser Antilles). *J. Volcanol. Geotherm. Res.* 51, 95–114.  
675 [https://doi.org/10.1016/0377-0273\(92\)90062-I](https://doi.org/10.1016/0377-0273(92)90062-I).

676 Bernard, M.L., Zamora, M., Géraud, Y., Boudon, G, 2007. Transport Properties of Pyroclastic  
677 Rocks from Montagne Pelée Volcano (Martinique, Lesser Antilles). *J. Geophys. Res.*, 112  
678 (B5).

679 Björbsson, G., Bodvarsson, G., 1990. A survey of geothermal reservoir properties.  
680 Geothermics. 19, 17–27.

681 Boitnott, G.N., Boyd, P.J., 1996. Permeability, electrical impedance, and acoustic velocities  
682 on reservoir rocks from the Geysers geothermal field. Proceedings of the Twenty-First  
683 Workshop on Geothermal Reservoir Engineering. Stanford University, Stanford,  
684 California. January 22-24. 1996.

685 Bonnet, M., Sardini, P., Billon, S., Siitari-Kauppi, M., Kuva, J., Fonteneau, L., Caner, L.  
686 2020. Determining crack aperture distribution in rocks using the <sup>14</sup>C-PMMA  
687 autoradiographic method: experiments and simulations. J. Geophys. Res., 125,  
688 e2019JB018241.

689 Bouysse, P., Westercamp, D., 1990. Subduction of atlantic aseismic ridges and late Cenozoic  
690 evolution of the Lesser Antilles Island Arc. Tectonophysics. 175, 349357–380.

691 Browne, P.R.L., 1978. Hydrothermal alteration in active geothermal fields. Ann Rev. of Earth  
692 and Planetary Sci. 6, 229–48.

693 Cai, J., Wei, W., Hu, X., Wood, D.A., 2017. Electrical conductivity models in saturated  
694 porous media: a review. Earth Sci. Rev. 171, 419–33.

695 Caldwell, G., Pearson, C. Zayadi, H. 1986. Resistivity of rocks in geothermal systems: a  
696 laboratory study. In proceedings 8th NZ geothermal workshop, 227–31.

697 Chapman, D.L., 1913. LI. A Contribution to the Theory of Electrocapillarity. The London,  
698 Edinburgh, and Dublin Philosophical Magazine and Journal of Science 25 (148): 475–81.

699 Coppo, N., Baltassat, J.M., Girard, J.F., Jacob, T., Martelet, G., Mathieu, F. and Wawrzyniak,  
700 P., 2014. Exploration géophysique (magnétotellurique et gravimétrie) du potentiel  
701 géothermique de La Martinique (Montagne Pelée, Anses d’Arlet, Pitons Du Carbet et  
702 Lamentin). Final report (in French). RP-62745-FR. BRGM. 278.

703 Cormy, G., Demians d'Archimbaud, J., Surcin, J., 1970. Prospection géothermique aux  
704 Antilles Françaises, Guadeloupe et Martinique. *Geothermics*. 2, 57–72.

705 Cosenza, P., Ghorbani, A., Florsch, N., Revil, A. 2007. Effects of drying on the low-  
706 frequency electrical properties of Tournemire argillites. *Pure Appl. Geophys.* 164, 2043-  
707 2066.

708 De Maisonneuve, C.B., Bachmann, O. and Burgisser, A., 2009. Characterization of juvenile  
709 pyroclasts from the Kos Plateau Tuff (Aegean Arc): insights into the eruptive dynamics of  
710 a large rhyolitic eruption. *Bul. Volcanol.* 71, 643.

711 Degruyter, W., Bachmann, O. and Burgisser, A., 2010. Controls on magma permeability in  
712 the volcanic conduit during the climactic phase of the Kos Plateau Tuff eruption (Aegean  
713 Arc). *Bul. Volcanol.* 72, .63.

714 Delayre C. 2018. Couplages altérations hydrothermales du caprock / propriétés  
715 pétrophysiques des roches en contexte géothermal de haute enthalpie. PhD thesis,  
716 University of Poitiers (France) (in French).

717 Dobson, P.F., Kneafsey, T.J., Hulen, J., Simmons, A., 2003. Porosity, permeability, and fluid  
718 flow in the Yellowstone geothermal system, Wyoming. *J. Volcanol. Geotherm. Res.* 123,  
719 313–24.

720 Escobedo, D., 2018. Study of hydrothermal alteration and petrophysical properties of well  
721 KH6 Krafla geothermal field, NE Iceland. Internship Geosciences Montpellier, 60p.

722 Farquharson, J., Heap, M.J., Varley, N.R., Baud, P. and Reuschlé, T., 2015. Permeability and  
723 porosity relationships of edifice-forming andesites: a combined field and laboratory study.  
724 *J. Volcanol. Geotherm. Res.* 297, 52-68.

725 Flóvenz, ÓG., Spangenberg, E., Kulenkampff, J., Árnason, K., Karlsdóttir, R. Huenges, E.,  
726 2005. The role of electrical interface conduction in geothermal exploration. Proceedings  
727 World Geothermal Congress 2005, Antalya, Turkey, 24-29 April 2005, 24–29.

728 Franklin, J.A., Vogler U.W., Szlavín, J., Edmond, J.M. Z.T. Bieniawski. 1981. Suggested  
729 methods for the determining water content, porosity, density, absorption and related  
730 properties and swelling and slake-durability index properties. In ISRM Suggested  
731 Methods: Rock Characterisation, Testing and Monitoring, Pergamon Press.

732 Frolova, J., Ladygin, V. Rychagov, S., 2001. Geothermal reservoir study through  
733 petrophysical data. Geothermal Resources Council Transactions. 25, 401–3.

734 Frolova, J., Ladygin, V. Rychagov, S., 2006. Petrophysical properties of argillitization zone in  
735 geothermal fields. Geothermal Resource Council Transactions. 30, 909–12.

736 Frolova, J., Gvozdeva, I.P., Kuznetsov, N.P., 2015. Effects of hydrothermal alterations on  
737 physical and mechanical properties of rocks in the Geysers Valley (Kamchatka Peninsula)  
738 in connection with landslide development. Proceedings World Geothermal Congress 2015  
739 Melbourne, Australia, 19-25 April 2015, 1–6.

740 Frolova, J.V., Ladygin, V.M. Rychagov, S.N., 2010. Petrophysical alteration of volcanic  
741 Rocks in hydrothermal systems of the Kuril-Kamchatka Island Arc. Proceedings World  
742 Geothermal Congress 2010 Bali, Indonesia, 25-29 April 2010.

743 Gadalia, A., Baltassat J.M., Bouchot, V., Caritg, S., Coppo, N., Gal, F., Girard, J.F.,  
744 Gutierrez, A., Jacob, T. Martelet, G., 2014. Compléments d’exploration géothermique en  
745 Martinique: conclusions et recommandations pour les zones de La Montagne Pelée, des  
746 Anses d’Arlet, des Pitons du Carbet et du Lamentin, 2014. Final Report (in French).  
747 BRGM/RP-FR 227.

748 Gadalia, A., Baltassat J.M., Bouchot, V., Caritg-Monnot, S., Gal, F., Girard J.F., Gutierrez A.,  
749 Jacob T., Martelet G., Coppo N., Rad S., Tailame A.L., Traineau H., Vittecoq B.,  
750 Wawrzyniak P., 2015. The Petite Anse-Diamant geothermal system (Martinique Island,  
751 Lesser Antilles): Results of the 2012-2013 exploration. Proceedings of World Geothermal  
752 Congress 2015. Melbourne, Australia. <https://hal-brgm.archives-ouvertes.fr/hal-01102469>.



753 Genter, A., Roig, J.Y., 2003. Réévaluation du potentiel géothermique dans les régions de  
754 Morne Rouge - Montagne Pelée et du Diamant (Martinique): Étude Géologique. Report  
755 RP-52546-FR. BRGM (in French).

756 Gerber, L., Maréchal, F., 2012. Environomic optimal configurations of geothermal energy  
757 conversion systems: application to the future construction of enhanced geothermal systems  
758 in Switzerland. *Energy*, 45, 908–23.

759 Germa, A., Quidelleur X., Labanieh S., Chauvel C., Lahitte, P., 2011. The volcanic evolution  
760 of Martinique Island: insights from K–Ar dating into the Lesser Antilles Arc migration  
761 since the Oligocene. *J. Volcanol. Geotherm. Res.* 208, 122–35.

762 Gonzales, K., Finizola, A., Lénat, J.F., Macedo, O., Ramos, D., Thouret, J.C., Fournier, N.,  
763 Cruz, V. Pistre, K., 2014. Asymmetrical structure, hydrothermal system and edifice  
764 stability: the case of Ubinas volcano, Peru, revealed by geophysical surveys. *J. Volcanol.*  
765 *Geotherm. Res.* 276: 132–44.

766 Ghorbani, A., Revil, A., Coperey, A., Ahmed, A. S., Roque, S., Heap, M. J., Grandis H.  
767 Viveiros, F. 2018. Complex conductivity of volcanic rocks and the geophysical mapping of  
768 alteration in volcanoes. *J. Volcanol. Geotherm. Res.* 357, 106-127.

769 Gouy, M. 1910. Sur la constitution de la charge électrique à la surface d'un électrolyte. *J.*  
770 *Phys. Theor. Appl.* 9 (1): 457–68.

771 Hang, P.T. Brindley, G.W., 1970. Methylene blue absorption by clay minerals. Determination  
772 of surface areas and cation exchange capacities (clay-organic studies XVIII). *Clays Clay*  
773 *Min.* 18, 203–12.

774 Heap, M.J. and Kennedy, B.M. 2016. Exploring the scale-dependent permeability of fractured  
775 andesite. *Earth Planet. Sci. Lett.* 447,139–150.

776 Heap, M.J., Kennedy, B.M., Farquharson, J.I., Ashworth, J., Mayer, K., Letham-Brake, M.,  
777 Reuschlé, T., Gilg, H.A., Scheu, B., Lavallée, Y. and Siratovich, P., 2017. A

778 multidisciplinary approach to quantify the permeability of the Whakaari/White Island  
779 volcanic hydrothermal system (Taupo Volcanic Zone, New Zealand). *J. Volcanol.*  
780 *Geotherm. Res.* 332, 88-108.

781 Heap, M.J., Troll, V.R., Kushnir, A.R., Gilg, H.A., Collinson, A.S., Deegan, F.M.,  
782 Darmawan, H., Seraphine, N., Neuberg, J. and Walter, T.R., 2019. Hydrothermal alteration  
783 of andesitic lava domes can lead to explosive volcanic behaviour. *Nature com.* 10, 1-10.

784 Heap, M.J., Gravley, D.M., Kennedy, B.M., Gilg, H.A., Bertollett, E. and Barker, S.L., 2020.  
785 Quantifying the role of hydrothermal alteration in creating geothermal and epithermal  
786 mineral resources: the Ohakuri ignimbrite (Taupō Volcanic Zone, New Zealand). *J.*  
787 *Volcanol. Geotherm. Res.*, <https://doi.org/10.1016/j.jvolgeores.2019.106703>.

788 Hellmuth, K.H., Siitari-Kauppi, M., 1990. Investigation of the porosity of rocks: impregnation  
789 with <sup>14</sup>C-Polymethylmethacrylate (PMMA), a new technique. Helsinki: Finnish Centre for  
790 Radiation and Nuclear Safety : Finnish Government Printing Centre. ISBN 9517-3949-3.

791 Hellmuth, K.H., Siitari-Kauppi M. Lindberg A., 1993. Study of porosity and migration  
792 pathways in crystalline rock by impregnation with <sup>14</sup>C-Polymethylmethacrylate. *J.*  
793 *Contaminant Hydrol.* 13, 403–18. [https://doi.org/10.1016/0169-7722\(93\)90073-2](https://doi.org/10.1016/0169-7722(93)90073-2).

794 Henley, R.W. Ellis, A.J., 1983. Geothermal systems ancient and modern: a geochemical  
795 review. *Earth Sci. Rev.* 19, 1–50.

796 Hughes, J.C., 1980. Crystallinity of kaolin minerals and their weathering sequence in some  
797 soils from Nigeria, Brazil and Colombia. *Geoderma* 24, 317–25.  
798 [https://doi.org/10.1016/0016-7061\(80\)90059-2](https://doi.org/10.1016/0016-7061(80)90059-2).

799 Inoue, A. 1995. Formation of Clay Minerals in Hydrothermal Environments. In: B. Velde  
800 (Ed.), *Origin and Mineralogy of Clays*, 268–329. Berlin, Heidelberg: Springer Berlin  
801 Heidelberg. [https://doi.org/10.1007/978-3-662-12648-6\\_7](https://doi.org/10.1007/978-3-662-12648-6_7).

802 Jayawardena, U.S. Izawa, E., 1994a. Application of present indices of chemical weathering  
803 for Precambrian metamorphic rocks in Sri Lanka. Définition d'indices d'altération pour  
804 des roches métamorphiques Précambriennes, Sri Lanka. Bull. Int. Ass. Eng. Geol. 49, 55.

805 Jayawardena, U.S. Izawa, E., 1994b. A new chemical index of weathering for metamorphic  
806 silicate rocks in tropical regions: a study from Sri Lanka. Eng. Geol., 36, 303–10.

807 Kagel, A. Gawell, K., 2005. Promoting geothermal energy: air emissions comparison and  
808 externality analysis. The Electricity J., 18, 90–99.

809 Kahr, G., Madsen, F.T., 1995. Determination of the cation exchange capacity and the surface  
810 area of bentonite, illite and kaolinite by methylene blue adsorption. Appl. Clay Sci. 9, 327–  
811 36.

812 Kanaya, K., Okayama, S., 1972. Penetration and energy-loss theory of electrons in solid  
813 targets.” J. Phys. D: Appl. Phys. 5, 43.

814 Komori, S., Kagiya, T., Hoshizumi, H., Takakura, S., Mimura, M., 2010. Vertical mapping  
815 of hydrothermal fluids and alteration from bulk conductivity: simple interpretation on the  
816 USDP-1 Site, Unzen Volcano, SW Japan. J. Volcanol. Geotherm. Res. 198, 339–47.

817 Kristinsdóttir, L.H., Flóvenz, Ó.G., Árnason, K., Bruhn, D., Milsch, H., Spangenberg, E.  
818 Kulenkampff, J., 2010. Electrical conductivity and P-Wave velocity in rock samples from  
819 high-temperature icelandic geothermal fields. Geothermics. 39, 94–105.

820 Lévy, L., Gibert, B. Sigmundsson, F. Flóvenz, Ó. G. Hersir, G. P. Briole, P., Pezard, P. A.  
821 2018. The role of smectites in the electrical conductivity of active hydrothermal systems:  
822 electrical properties of core samples from Krafla volcano, Iceland. Geophys. J. Intern. 215,  
823 1558-1582.

824 Lévy, L., Maurya, P. K., Byrdina, S., Vandemeulebrouck, J., Sigmundsson, F., Arnason, K.,  
825 Ricci T., Deldicque D., Roger M., Gibert, B., Labazuy, P. 2019. Electrical resistivity  
826 tomography and time-domain induced polarization field investigations of geothermal areas

827 at Krafla, Iceland: comparison to borehole and laboratory frequency-domain electrical  
828 observations. *Geophys. J. Intern.* 218, 1469-1489.

829 Lorenz, P.M. 1999. Determination of the cation exchange capacity (CEC) of clay minerals  
830 using the complexes of copper (II) ion with triethylenetetramine and  
831 tetraethylenepentamine. *Clays Clay Miner.* 47, 386–88.

832 Macdonald, R., Hawkesworth, C.J., Heath, E., 2000. The Lesser Antilles volcanic chain: a  
833 study in arc magmatism. *Earth Sci. Rev.* 49, 1–76. [https://doi.org/10.1016/S0012-](https://doi.org/10.1016/S0012-8252(99)00069-0)  
834 [8252\(99\)00069-0](https://doi.org/10.1016/S0012-8252(99)00069-0).

835 Mayer, K., Scheu, B., Montanaro, C., Yilmaz, T.I, Isaia, R., Aßbichler, D. Dingwell, D.B.,  
836 2016. Hydrothermal alteration of surficial rocks at Solfatara (Campi Flegrei): petrophysical  
837 properties and implications for phreatic eruption processes *J. Volcanol. Geotherm. Res.*  
838 320, 128–43.

839 Mazurier, A., Sardini, P., Rossi, A. M., Graham, R. C., Hellmuth, K. H., Parneix, J. C.,  
840 Sitaari-Kaupi, M., Voutilainen, M., Caner, L. 2016. Development of a fracture network in  
841 crystalline rocks during weathering: Study of Bishop Creek chronosequence using X-ray  
842 computed tomography and <sup>14</sup>C-PMMA impregnation method. *GSA Bul.*, 128(9-10),  
843 1423-1438.

844 Meunier, A., Beaufort, D., 2017. Clay minerals in hydrothermal systems. *Geochimica*  
845 *Brasiliensis* 10, 347–63.

846 Mielke, P, Prieto, A.M., Bignall, G. Sass, I., 2015. Effect of hydrothermal alteration on rock  
847 properties in the Tauhara Geothermal Field, New Zealand. *Proceedings World Geothermal*  
848 *Congress 2015 Melbourne, Australia, 19-25 April 2015*.

849 Milsch, H., Blöcher, G., Engelmann, S., 2008. The relationship between hydraulic and  
850 electrical transport properties in sandstones: An experimental evaluation of several scaling  
851 models. *Earth Planet. Sci. Lett.* 275, 355–63.

852 Mordensky, S.P., Villeneuve, M.C., Kennedy, B.M., Heap, M.J., Gravley, D.M., Farquharson,  
853 J.I., Reushlé, T. 2018. Physical and mechanical property relationships of a shallow  
854 intrusion and volcanic host rock, Pinnacle Ridge, Mt. Ruapehu, New Zealand. *J. Volcanol.*  
855 *Geotherm. Res.* 359, 1–20.

856 Mordensky, S.P., Kennedy, B.M., Villeneuve, M.C., Lavallée, Y., Reichow, M.K., Wallace,  
857 P.A., Siratovich, P.A. and Gravley, D.M., 2019. Increasing the permeability of  
858 hydrothermally altered andesite by transitory heating. *Geochem. Geophys. Geosys.* 20,  
859 5251-5269.

860 Muñoz, G. 2014. Exploring for geothermal resources with electromagnetic methods. *Surv.*  
861 *Geophys.* 35, 101–22. <https://doi.org/10.1007/s10712-013-9236-0>.

862 Navelot, V., Géraud, Y., Favier, A., Diraison, M., Corsini, M., Lardeaux, J. M., Verati C,  
863 Mercier de Lépinay J. Legendre L., .Beauchamps, G. 2018. Petrophysical properties of  
864 volcanic rocks and impacts of hydrothermal alteration in the Guadeloupe Archipelago  
865 (West Indies). *J. Volcanol. Geotherm. Res.* 360, 1-21.

866 Nielson, D. L., Clemente, W. C., Moore, J. N., Powell, T. S. 1996. Fracture permeability in  
867 the Matalibong-25 corehole, Tiwi geothermal field, Philippines (No. SGP-TR-151-30).  
868 Earth Sciences and Resources Institute, University of Utah, Salt Lake City, UT; Philippine  
869 Geothermal, Inc., Metro Manila, PH; Unoal Energy Resources Division, Santa Rosa, CA.

870 Nehler, M., Andolfsson, T., Stöckhert, F., Renner, J., Bracke, R. 2016. Monitoring fluid-rock  
871 interactions at In-Situ conditions using computed tomography. In *Proceedings, 41st*  
872 *Workshop on Geothermal Reservoir Engineering, Stanford University, Stanford,*  
873 *California, 22–24th 2010, SGP-TR-209.*

874 O’Sullivan, M.J., Pruess, K. Lippmann, M.J., 2001. State of the art of geothermal reservoir  
875 simulation. *Geothermics.* 30, 395–429.

876 Patrier, P., Papapanagiotou, P., Beaufort, D., Traineau, H., Bril, H., and Rojas, J., 1996. Role  
877 of permeability versus temperature in the distribution of the fine (< 0.2 Mm) clay fraction  
878 in the Chipilapa geothermal system (El Salvador, Central America). *J. Volcanol.*  
879 *Geotherm. Res.* 72, 101–20. [https://doi.org/10.1016/0377-0273\(95\)00078-X](https://doi.org/10.1016/0377-0273(95)00078-X).

880 Petrov, V.A., Poluektov, V.V., Zharikov, A.V., Velichkin, V.I., Nasimov, R.M., Diaur,  
881 N.I., Terentiev, V.A., Shmonov, V.M., Vitovtova, V.M. 2005. Deformation of  
882 metavolcanics in the Karachay Lake area, Southern Urals: petrophysical and mineral—  
883 chemical aspects. In P.K. Harvey, P.A. Pezard, T.S. Brewer, V.A. Petrov (eds).  
884 *Petrophysical properties of crystalline rock. Geological Society special publication 20.*  
885 <https://doi.org/10.1144/GSL.SP.2005.240.01.22>.

886 Pirajno, F., 2009. Hydrothermal processes associated with meteorite impacts. In  
887 *Hydrothermal Processes and Mineral Systems*, 1097–1130. Springer.

888 Pirrie, D., Butcher, A.R., Power, M.R., Gottlieb, P. Miller, G.L., 2004. Rapid quantitative  
889 mineral and phase analysis using automated scanning electron microscopy (QemSCAN);  
890 potential applications in forensic geoscience.” Geological Society, London, Special  
891 *Publications 232 (1): 123–36.* <https://doi.org/10.1144/GSL.SP.2004.232.01.12>.

892 Pola, A., Crosta, G., Fusi, N., Barberini, V., Norini, G. 2012. Influence of alteration on  
893 physical properties of volcanic rocks. *Tectonophys.* 566, 67-86.

894 Pola, A., Crosta, G. B., Fusi, N., Castellanza, R., 2014. General characterization of the  
895 mechanical behaviour of different volcanic rocks with respect to alteration. *Eng. Geol.* 169,  
896 1-13.

897 Pola, A., Martínez-Martínez, J., Macías, J. L., Fusi, N., Crosta, G., Garduño-Monroy, V. H.,  
898 Núñez-Hurtado, J. A. 2016. Geomechanical characterization of the Miocene Cuitzeo  
899 ignimbrites, Michoacán, Central Mexico. *Eng. Geol.* 214, 79-93.

900 Pruess, K., 1990. Modeling of geothermal reservoirs: fundamental processes, computer  
901 simulation and field applications. *Geothermics*. 19, 3–15.

902 Revil, A. Glover P.W.J., 1998. Nature of Surface Electrical Conductivity in Natural Sands,  
903 Sandstones, and Clays. *Geophys. Res. Lett.* 25, 691–94.

904 Revil, A, Hermitte, D., Spangenberg, E. Cochémé, J.J., 2002. Electrical properties of  
905 zeolitized volcanoclastic materials. *J. Geophys. Res.: Solid Earth*, 107 (B8).

906 Revil, A., Murugesu, M., Prasad, M., Le Breton, M. 2017. Alteration of volcanic rocks: A  
907 new non-intrusive indicator based on induced polarization measurements. *J. Volcanol.*  
908 *Geotherm. Res.* 341, 351-362.

909 Revil, A., Qi, Y., Ghorbani, A., Ahmed, A. S., Ricci, T., Labazuy, P. 2018a. Electrical  
910 conductivity and induced polarization investigations at Krafla volcano, Iceland. *J.*  
911 *Volcanol. Geotherm. Res.* 368, 73-90.

912 Revil, A., Ghorbani, A., Gailler, L. S., Gresse, M., Cluzel, N., Panwar, N., Sharma, R. 2018b.  
913 Electrical conductivity and induced polarization investigations at Kilauea volcano, Hawai'i.  
914 *J. Volcanol. Geotherm. Res.* 368, 31-50.

915 Roberson, H.E., Lahann, R.W., 1981. Smectite to illite conversion rates: effects of solution  
916 chemistry. *Clays Clay Min.* 29, 129–35.

917 Rybach, L. 2010. The future of geothermal energy and its challenges. *Proceedings World*  
918 *Geothermal Congress 2010 Bali, Indonesia, 25-29 April 2010.*

919 Sammartino, S., Partier, P., Sardini, P., Meunier, A., Tevissen, E., 1999. Evolution of fluid  
920 pathways of Charroux-Civary Tonalite (Part I): alteration effects—an analytical approach.  
921 *Phys. Chem. Earth, Part A: Solid Earth and Geodesy.* 24, 601–6.

922 Sanjuan, B., Romain, M., Michel, B., Foucher, J.C., Roig, J.Y., Baltassat, J.M., 2005.  
923 Geothermal exploration in the Mount Pelée volcano-Morne Rouge and Diamant areas

924 (Martinique, West French Indies): geochemical data. Proceedings World Geothermal  
925 Congress 2005 Antalya, Turkey, 24-29 April 2005.

926 Santamarina, J.C., Klein, K.A., Wang, Y.H., Prencke, E., 2002. Specific surface:  
927 determination and relevance. *Canadian Geotech. J.* 39, 233–41.

928 Sardini, P., B. Ledésert, G. Touchard, Quantification of microscopic networks by image  
929 analysis and measurement of the permeability of the Soultz-sous-Forêts granite (Alsace,  
930 France). *Conference Volume of the 9th Kongsberg Seminar, Fluid Flow and Transport in  
931 Rocks*, 3-5 mai 1995, Chapman et al. (B. Jamtveit & B. Yardley eds), pp. 171-189, 1996.

932 Shainberg, I., Rhoades, J.D., Prather, R.J., 1980. Effect of exchangeable sodium percentage,  
933 cation exchange capacity, and soil solution concentration on soil electrical conductivity.  
934 *Soil Sci. Soc. Am. J.* 44, 469–73.

935 Siitari-Kauppi, M., 2002. Development of <sup>14</sup>C-Polymethylmethacrylate method for the  
936 characterisation of low porosity media. Application to rocks in geological barriers of  
937 nuclear waste storage. Ph. D. Thesis of the University of Poitiers (France) and the  
938 University of Helsinki (Finland).

939 Stern, O., 1924. Zur theorie der elektrolytischen doppelschicht. *Berichte Der  
940 Bunsengesellschaft Für Physikalische Chemie.* 30, 508–16.

941 Stimac, J.A., Powell, T.S., Golla, G.U., 2004. Porosity and permeability of the Tiwi  
942 geothermal field, Philippines, based on continuous and spot core measurements.  
943 *Geothermics.* 33, 87–107.

944 Tester, J.W., Anderson B.J., Batchelor, A.S., Blackwell, D.D., DiPippo, R., Drake, E.,  
945 Garnish, J., Livesay, B., Moore, M.C., Nichols, K., 2006. The future of geothermal  
946 energy. *Impact of Enhanced Geothermal Systems (EGS) on the United States in the 21st  
947 Century.* Massachusetts Institute of Technology, Cambridge, MA, 372.



948 Traineau, H, Bouchot, V., Caritg, S., Gadalia, A., 2013. Compléments d'exploration  
949 géothermique en Martinique: volet géologie, Rapport Intermédiaire. BRGM/RP-62349-FR.  
950 BRGM (in French).

951 Udagedara, D.T., Oguchi C.T. Gunatilake, J.K., 2017. Evaluation of geomechanical and  
952 geochemical properties in weathered metamorphic rocks in tropical environment: a case  
953 study from Samanalawewa hydropower project, Sri Lanka. Geosci. J. 21, 441–52.

954 Ussher, G., Harvey, C., Johnstone, R., Anderson, E., 2000. Understanding the resistivities  
955 observed in geothermal systems. Proceedings World Geothermal Congress 2000 Kyushu -  
956 Tohoku, Japan, May 28 - June 10, 2000.

957 Waxman, M.H., Smits, L.J.M., 1968. Electrical conductivities in oil-bearing shaly sands. Soc.  
958 Petrol. Eng. J. 8, 107–22.

959 White, N.C., Hedenquist, J.W., 1990. Epithermal environments and styles of mineralization:  
960 variations and their causes, and guidelines for exploration. J. Geochem. Explor. 36, 445–  
961 74.

962 Wollentz, K. and Heiken, G. 1992. Volcanology and geothermal energy. Univ. of California  
963 press. <http://ark.cdlib.org/ark:/13030/ft6v19p151/>.

964 Wright, H.M.N., Cashman, K.V., Gottesfeld, E.H., Roberts, J.J., 2009. Pore structure of  
965 volcanic clasts: measurements of permeability and electrical conductivity. Earth Planet.  
966 Sci. Lett. 280, 93–104.

967 Wyering, L.D., Villeneuve, M. Wallis, I., 2012. The effects of hydrothermal alteration on  
968 mechanical rock properties of the Andesite Breccia and Tahorakuri Formation from the  
969 Ngatamariki geothermal field, New Zealand and empirical relations between rock strength  
970 and physical properties. Proceedings of New Zealand geothermal workshop, Auckland,  
971 New Zealand (34). <https://www.geothermal-library.org>. 2012.

972 Wyering, L.D., Villeneuve, M.C., Wallis, I.C., Siratovich, P.A., Kennedy, B.M., Gravley,  
973 D.M. and Cant, J.L., 2014. Mechanical and physical properties of hydrothermally altered  
974 rocks, Taupo volcanic zone, New Zealand. *J. Volcanol. Geotherm. Res.* 288, 76–93.

975 Yukselen, Y., and Kaya, A., 2008. Suitability of the methylene blue test for surface area,  
976 cation exchange capacity and swell potential determination of clayey soils. *Eng.Geol.* 102,  
977 38–45.

978

979 **Figure captions**

980 Figure 1: Locations of the Petite Anse-Diamant area on Martinique Island (A) and the  
981 samples investigated in this study (B). The red point (E-F) indicates the location of the Eaux-  
982 Ferrées thermal source (source: IGN, French institute of geography).

983 Figure 2: (A) Experimental setup for the permeability measurements (Sammartino et al.  
984 1999). (B) Cross-section of the permeability cell with (1) the pressure vessels of stainless  
985 steel, (2) the confining cell and (3) the plug sample. (C) Perspective view of the plug sample  
986 with the diameters of the core sample and plug opening (mm).

987 Figure 3: Resistivity cell used for acquisition of the impedance spectra.

988 Figure 4: QEMSCAN® mineral maps of samples PA13.2, PA13.1, PA4, PA 7.2, PA10.1,  
989 PA12 and PA 11. White areas are pixels detected as porosity. Sample PA13 is the freshest  
990 sample of andesite, presenting moderate alteration of hornblende to montmorillonite at the  
991 bottom of the section (arrow 3), and silica and oxides abundance in the mesostase (arrows 1  
992 and 2). In sample PA4, intragranular alteration of hornblende crystals is underscored by  
993 montmorillonite and oxides in cleavage planes. Sample PA10.1 exhibits pervasive alteration  
994 of the mesostase (presence of montmorillonite, silica, and sulphide minerals) (arrows 1,2). In  
995 sample PA12, hornblende crystals are totally replaced by montmorillonite and iron oxides  
996 (arrow 1); carbonate veins are also detected (arrow 2). Sample PA11 is extremely altered;  
997 hornblende is totally replaced by silica and montmorillonite (arrow 3), and feldspars  
998 phenocrysts are partially dissolved, containing dissolution voids( arrow 2), which are partially  
999 filled with kaolinite and silica (arrow 1). In this sample, quartz grains remains unaltered.

1000 Figure 5: Correlation plot between the abundances of the clay phases identified by the  
1001 QEMSCAN® system and the crystal lattice water proportions obtained from bulk-rock  
1002 chemical analysis. Mt = montmorillonite and K = kaolinite.

1003 Figure 6: QEMSCAN® Mineral maps (left) and related autoradiographs (right) from the <sup>14</sup>C-  
1004 PMMA method of samples PA 13, PA 4, PA 10.1, PA 12 and PA 11. In autoradiographs, the  
1005 darker the grey level is, the higher the porosity is. In the freshest sample (PA13) the most  
1006 porous mineral is hornblende, partially replaced by montmorillonite in PA 13.1 side (arrow  
1007 1). In PA4 sample, porosity is well developed in hornblende cleavage planes (arrow 1), and  
1008 corresponds to montmorillonite; feldspars remains lowly porous (arrow 2). In sample PA  
1009 10.1, low porosity area are initial feldspar phenocrysts (arrow 2), but are also in sulphide of  
1010 pseudomorphosed hornblende (arrow1) and in carbonate cements. Montmorillonite-rich areas  
1011 and in a less extent mesostase present an higher porosity. In PA12, Feldspars remain unaltered  
1012 and lowly porous (arrow 1), as well carbonate. High porosity of pseudomorphosed hornblende  
1013 cannot be differentiate from the porosity of the mesostase (arrow 3).

1014 Sample PA11, which is the most affected by hydrothermal alteration, presents a totally  
1015 different porosity pattern than sample PA12. In this sample, quartz grains remains the only  
1016 lowly porous mineral (arrow 3). The connected mesostase matrix is porous, but  
1017 pseudomorphosed hornblende (arrow 1) and altered/dissolved feldspars associated with  
1018 dissolution voids (arrow 2) are more porous.

1019 Figure 7: (A) Plot of the connected porosity of the samples against the structural water  
1020 content ( $H_2O^+$ ) value obtained with the triple weight (TW) method and from bulk-rock  
1021 chemical analysis. The  $H_2O^+$  values are used as indicators of the clay mineral abundances (see  
1022 section 2.2). (B) Darcian permeability against the connected porosity.

1023 Figure 8: Bulk conductivities versus conductivities of the solutions saturating the samples.  
1024 The 1:1 line is used to estimate the isoconductivity point of each sample.

1025 Figure 9: Correlation plots of the bulk conductivity measured for the samples saturated with  
1026 the 2 wt % NaCl solution depending on the structural water proportion ( $H_2O^+$ ) (A) and blue  
1027 methylene (BM) value (B).

1028 Figure 10: Evolution of the isoconductivity point depending on the blue methylene (BM)  
1029 value.

1030

1031

1032

1033 **Table captions**

1034 Table 1: Description of color and consolidation of each samples.

1035 Table 2. Comparison of  $^{14}\text{C}$ -PMMA porosity method with conventional imaging methods.

1036 Table 3: Quantitative evaluation of rock mineral composition from QEMSCAN® analysis.

1037 Table 4: Crystal lattice water proportions ( $\text{H}_2\text{O}^+$ ) from bulk-rock chemical analysis; connected  
 1038 porosities  $\phi_w$  and  $\phi_{FA}$  obtained by triple-weighted method (TW) and from film  
 1039 autoradiography (FA) respectively and Darcian permeabilities  $k$  of samples.

1040 Table 5. Conductivities of the solutions saturating the samples and bulk conductivities  
 1041 (expressed in  $\mu\text{S}\cdot\text{cm}^{-1}$ ).

1042

1043

		Consolidation	Color	1044
	PA 1	good	grey	1045
	PA 2	good	grey	1046
PA 3	PA 3.1	good	grey	1047
	PA 3.2	good	red wall-rock (FeOx)	1048
	PA 4	good	grey	1049
	PA 5.1	moderate	grey yellowish	1050
	PA 7.2	moderate	whitish grey	1051
	PA 10.1	good	dark grey	1052
	PA 11	poorly consolidated	yellowish	1053
	PA 12	poorly consolidated	greenish	1054
PA13	PA 13.1	good	whitish grey	1055
	PA 13.2	very hard	red wall-rock (FeOx)	1056
				1057

1058 Table 1: Description of color and consolidation of each samples.

Porosimetric Method	Raw data	Connected/Total	Sample size	Advantages	Drawbacks
14C-PMMA (imaging)	2D porosity map from activity map and calibration	3D Connected	dm <sup>3</sup> to > cm <sup>3</sup>	<ul style="list-style-type: none"> <li>• Porosity map regardless of pore size.</li> <li>• Pore type distinction. 2D porosity mapping easy to analyse.</li> <li>• Fracture aperture distribution</li> </ul>	<ul style="list-style-type: none"> <li>• Use of radioactive resins.</li> <li>• Adaptation in development for swelling clay samples.</li> <li>• "Confidential" method.</li> <li>• Non applicable to naturally radioactive sample.</li> </ul>
XRCT (imaging)	3D map of resolved pores from X-Ray attenuation map	Total and/or 3D connected	dm <sup>3</sup> to mm <sup>3</sup>	<ul style="list-style-type: none"> <li>• 3D mapping of pores.</li> <li>• 3D pore size and geometry. 3D grid/mesh for transport modelling.</li> <li>• Good availability</li> </ul>	<ul style="list-style-type: none"> <li>• Data difficult to handle and complex to process.</li> <li>• Pore resolution depends on voxel size.</li> <li>• Segmentation of pores is often complicated.</li> <li>• Grey levels are not only a function of porosity</li> </ul>
SEM - BSE (imaging)	2D map of resolved pores from BSE images	Total	Thin section	<ul style="list-style-type: none"> <li>• Pore type distinction.</li> <li>• 2D mapping of pores</li> </ul>	<ul style="list-style-type: none"> <li>• Using large mosaic image, Data are heavy to handle. Pore resolution depends on pixel size.</li> <li>• Grey levels levels are not only a function of porosity.</li> </ul>
Gas adsorption methods BJH	Pore size distribution	3D Connected	mm <sup>3</sup>	<ul style="list-style-type: none"> <li>• Fast and widely used</li> </ul>	<ul style="list-style-type: none"> <li>• Pore size from 3 to 300 nm.</li> <li>• Not a porosity measurement technique.</li> </ul>
Hg-porosimetry	Bulk value and throat size distribution	3D Connected	cm <sup>3</sup>	<ul style="list-style-type: none"> <li>• Fast and widely used</li> </ul>	<ul style="list-style-type: none"> <li>• Not pore size, but throat size.</li> <li>• Toxicity of Hg.</li> </ul>

Water porosity by Triple Weighting	Bulk value	3D Connected	dm <sup>3</sup> to mm <sup>3</sup>	<ul style="list-style-type: none"> <li>• Fast and cheap.</li> <li>• Essential for controlling porosity from imaging methods</li> </ul>	<ul style="list-style-type: none"> <li>• Only bulk method.</li> <li>• Speed of water intrusion depend on rock water permeability, and can be long.</li> </ul>
He-Pycnometry	bulk value	3D Connected	cm <sup>3</sup> to mm <sup>3</sup>	<ul style="list-style-type: none"> <li>• Fast intrusion of He.</li> <li>• Cheap.</li> <li>• Essential for controlling porosity from imaging methods</li> </ul>	<ul style="list-style-type: none"> <li>• Only bulk.</li> <li>• Apparent volume should be known to determine porosity.</li> </ul>

1059 Table 2. Comparison of <sup>14</sup>C-PMMA porosity method with conventional imaging methods.



1060

1061

	PA 13.2	PA 13.1	PA 3.1	PA 10.1	PA 4	PA 7.2	PA 12	PA 11
Mesostasis	32.79	43.71	38.76	38.38	34.85	30.53	40.37	34.57
Andesine	16.87	17.23	20.68	19.27	21.49	20.85	13.81	2.81
Labradorite	12.59	13.64	13.97	10.64	12.92	13.22	5.89	0.24
Oligoclase	5.38	6.98	3.44	2.3	3.07	2.63	3.56	1.22
Bytownite	0.48	0.58	0.59	0.38	0.55	0.62	0.05	-
Hornblende	13.9	4.91	3.43	0.1	4.88	9.82	0.5	0.33
Montmorillonite	4.69	5.35	6.55	7.08	9.57	10.73	15.21	22.74
Kaolinite	0.99	0.69	0.68	1.01	0.94	1.02	3.92	14.82
Quartz/Silica	8.64	4.91	7.87	14.77	8.2	8.54	12.74	21.77
Calcite	-	-	1.46	1.91	0.01	-	2.39	-
Ankerite	-	-	0.08	-	0.37	-	-	-
Siderite	-	-	0.11	-	0.04	-	-	-
Dolomite	-	-	-	0.29	-	-	-	-
Magnetite	1.43	1.13	1.04	-	1.3	1.35	0.81	0.04
/Hematite+Ti								
Magnetite/Hematite	0.71	0.18	0.52	0.03	0.42	0.22	0.35	0.65
Ilmenite	0.17	0.08	0.18	0.2	0.1	0.07	0.21	0.23
Sulfide minerals	-	-	0.01	3.36	-	-	-	-
Apatite	0.13	0.13	0.17	0.14	0.18	0.19	0.09	-
Gypsum	0.05	0.07	-	-	-	-	-	0.02
Zircon	-	-	-	-	0.01	0.01	-	0.01
Rhodocrosite	-	-	-	0.03	0.52	-	-	-
Other minerals	1.16	0.4	0.05	0.03	0.03	0.01	0.06	0.56
Non identified	0.01	-	0.44	0.05	0.54	0.18	0.03	-

1062 Table 3: Quantitative evaluation of rock mineral composition from QEMSCAN® analysis.

1063

1064

	H <sub>2</sub> O <sup>+</sup> (wt%)	$\phi_{tw}$ (%)	$\phi_{FA}$ (%)	Permeability $k$ (m <sup>2</sup> )
PA 1	0.84	7.45	-	5.8 10 <sup>-19</sup>
PA 2	1.03	4.28	-	2.77e10 <sup>-19</sup>
PA 3.1	0.76	3.74	4.31	1.72 10 <sup>-17</sup>
PA 3.2	1.04	9.46	-	2.32 10 <sup>-19</sup>
PA 4	1.13	7.33	4.14	4.5 10 <sup>-19</sup>
PA 5.1	1.18	9.86	-	3.9e10 <sup>-19</sup>
PA 7.2	1.91	7.2	4.93	7.66 10 <sup>-20</sup>
PA 10.1	1.21	13.84	11.21	2.48 10 <sup>-18</sup>
PA 11	6.23	35.35	20.99	5.36 10 <sup>-17</sup>
PA 12	2.78	17.05	9.76	1.61 10 <sup>-17</sup>
PA 13.1	0.65	10.5	6.59	-
PA 13.2	0.93	4.48	4.11	-

1066 Table 4: Crystal lattice water proportions (H<sub>2</sub>O<sup>+</sup>) from bulk-rock chemical analysis; connected  
1067 porosities  $\phi_{tw}$  and  $\phi_{FA}$  obtained by triple-weighted method (TW) and from film  
1068 autoradiography (FA) respectively and Darcian permeabilities  $k$  of samples.

Solution	Sample Number									
	PA.1	PA.2.1.	PA.3.1	PA.3.2	PA .4	PA.5.1	PA.7.2	PA.10.1	PA.11	PA.12
219.40	70.900	87.000	78.700	181.00	81.700	202.90	112.30	486.90	1039.5	1256.3
995.40	87.400	N/A	97.100	246.50	104.80	263.90	147.20	687.00	1772.0	1380.0
1956.7	94.700	116.70	N/A	258.10	109.30	232.80	142.20	614.30	N/A	1428.0
9297.4	133.80	168.40	152.40	369.40	156.60	311.40	185.90	895.30	2283.1	2125.0
17599.0	202.30	263.40	248.00	539.70	237.10	223.00	286.30	1246.9	3236.2	2898.6
31288.0	267.70	366.80	313.50	719.40	326.90	557.40	397.90	1618.1	5434.8	3663.0

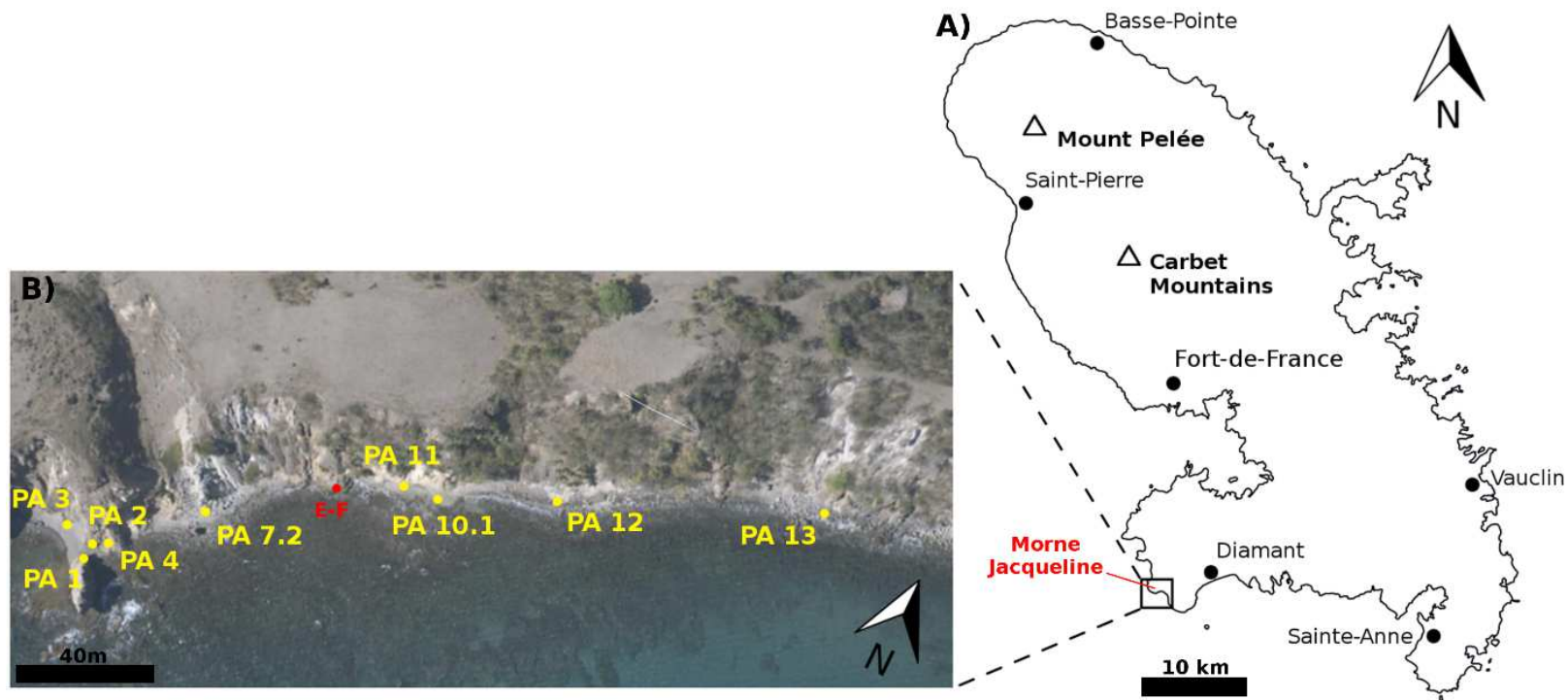
1070

1071 Table 5. Conductivities of the solutions saturating the samples and bulk conductivities (expressed in  $\mu\text{S}\cdot\text{cm}^{-1}$ ).

1072

1073

1074



1075

1076 Figure 1: Locations of the Petite Anse-Diamant area on Martinique Island (A) and the samples investigated in this study (B). The red point (E-F)

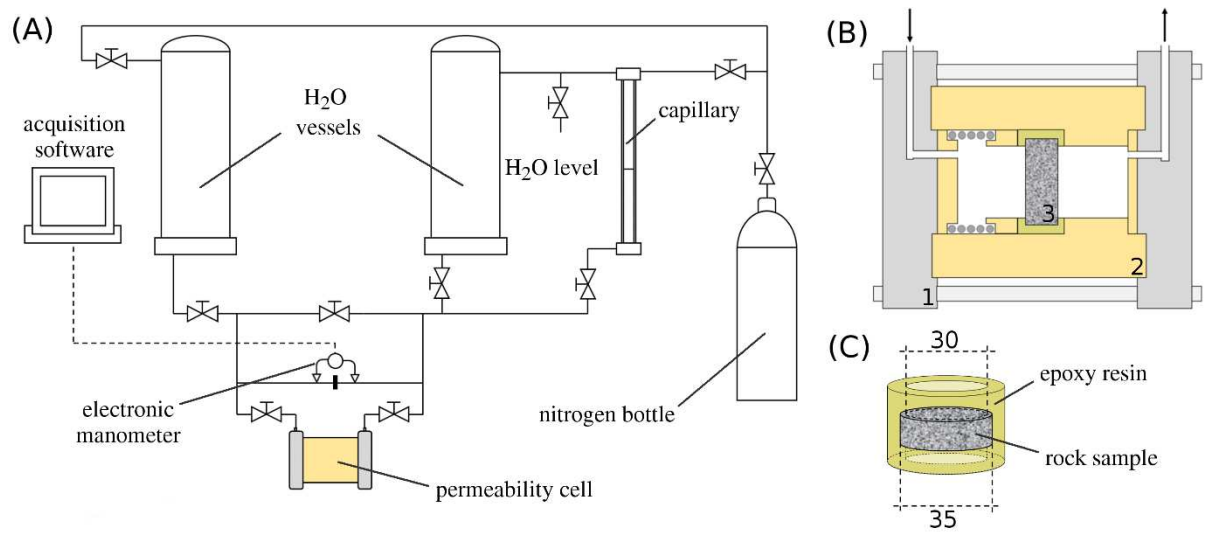
1077 indicates the location of the Eaux-Ferrées thermal source (source: IGN, French institute of geography).

1078

1079

1080

1081



1082

1083 Figure 2: (A) Experimental setup for the permeability measurements (Sammartino et al.

1084 1999). (B) Cross-section of the permeability cell with (1) the pressure vessels of stainless

1085 steel, (2) the cell core (in PEEK) and (3) the plug sample. (C) Perspective view of the plug

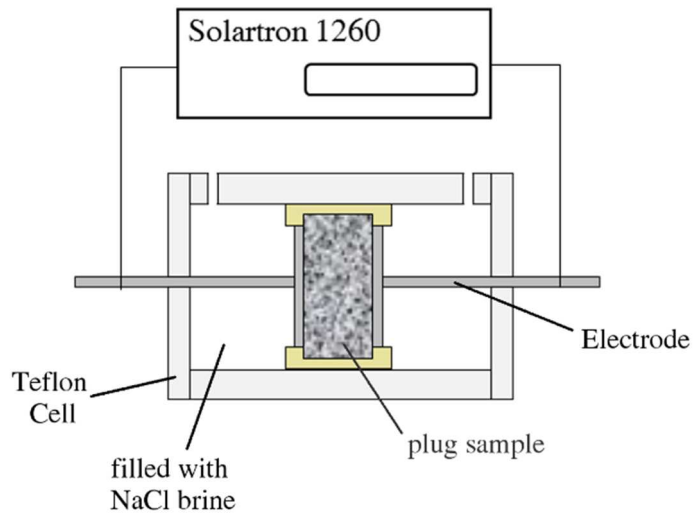
1086 sample with the diameters of the core sample and plug opening (mm).

1087

1088

1089

1090



1091  
1092

1093 Figure 3: Resistivity cell used for acquisition of the impedance spectra.

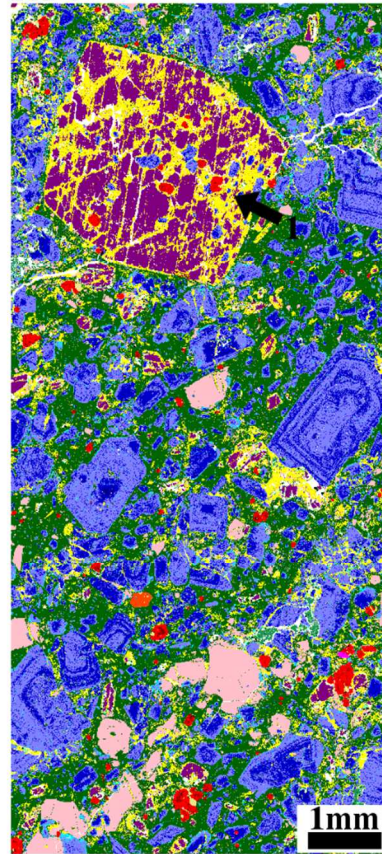
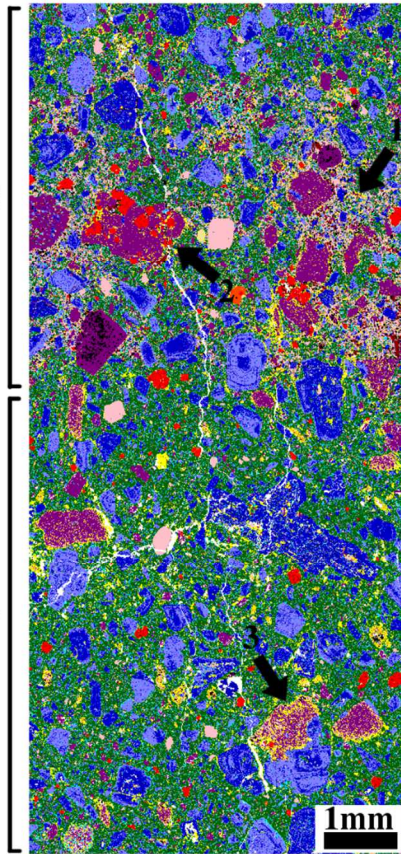
1094

1095

PA 13.2

PA 13.1

PA 4



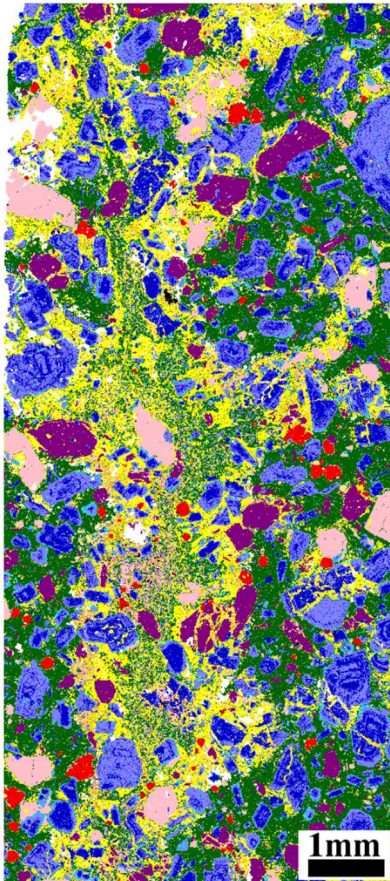
- Quartz
- Magnetite/Hematite
- Magnetite/Hematite + Ti
- Ilmenite
- Anorthite
- Bytownite
- Labradorite
- Andesine
- Oligoclase
- Hornblende
- Montmorillonite
- Kaolinite
- Zircon
- Other silicates
- Apatite
- Sulfide mineral
- Calcite
- Ankerite
- Siderite
- Dolomite
- Rhodocrosite
- Glass
- Gypsum
- Other mineral
- Non identified

1096

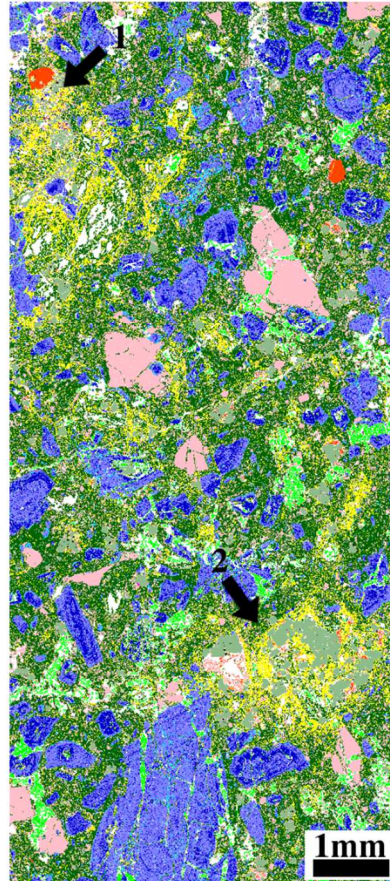
1097



PA 7.2

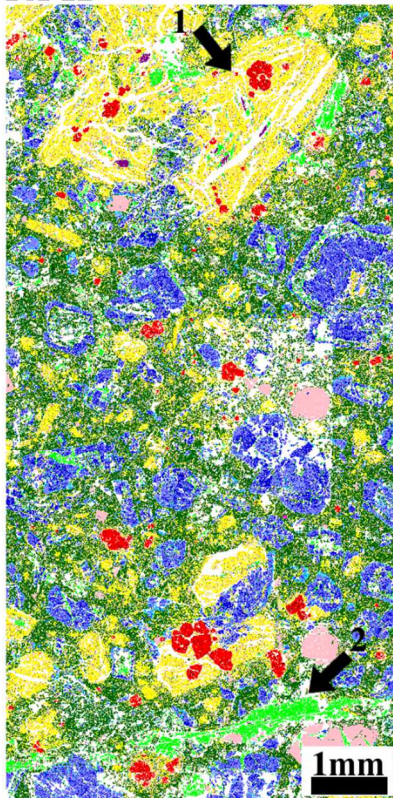


PA 10.1

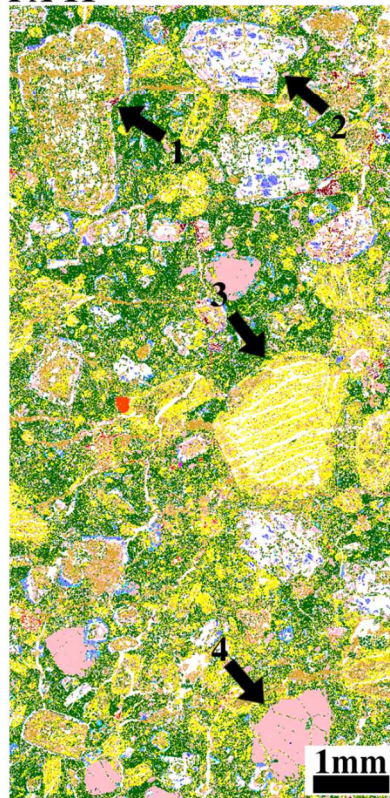


- Quartz
- Magnetite/Hematite
- Magnetite/Hematite + Ti
- Ilmenite
- Anorthite
- Bytownite
- Labradorite
- Andesine
- Oligoclase
- Hornblende
- Montmorillonite
- Kaolinite
- Zircon
- Other silicates
- Apatite
- Sulfide mineral
- Calcite
- Ankerite
- Siderite
- Dolomite
- Rhodocrosite
- Glass
- Gypsum
- Other mineral
- Non identified

PA 12

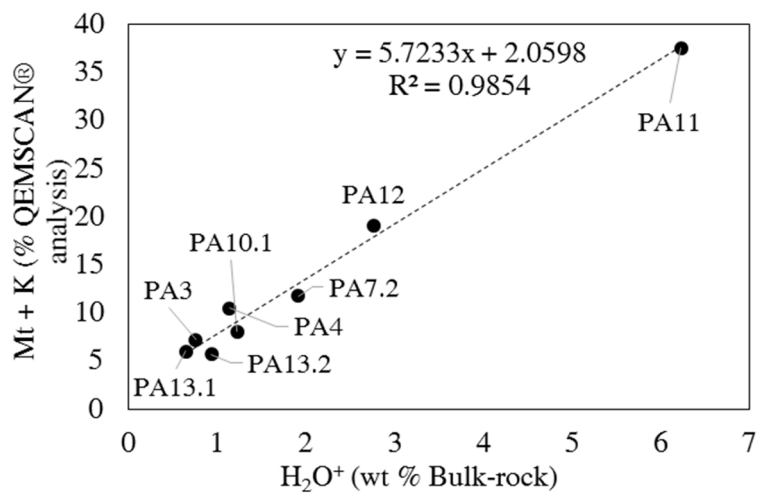


PA 11





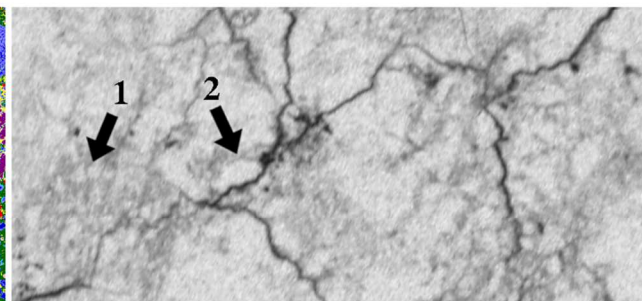
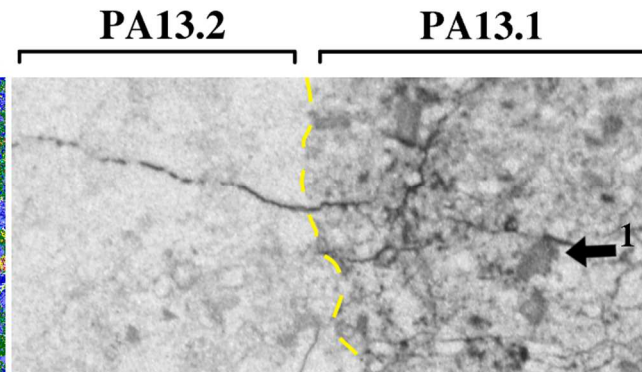
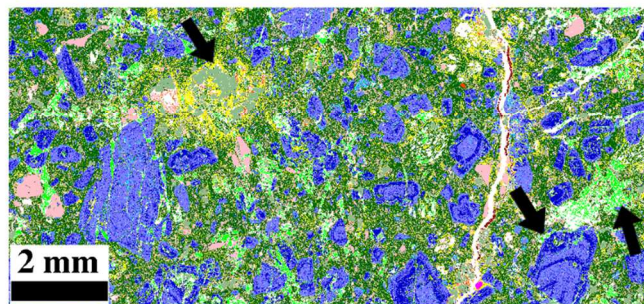
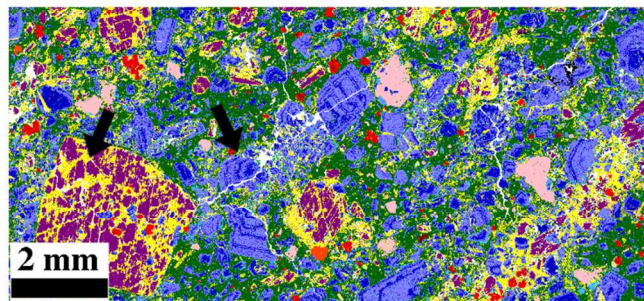
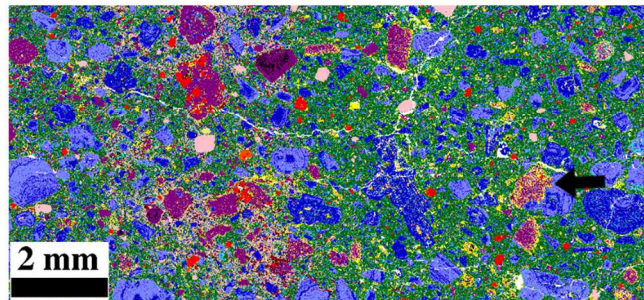
1099 Figure 4: QEMSCAN® mineral maps of samples PA13.2, PA13.1, PA4, PA 7.2, PA10.1,  
 1100 PA12 and PA 11. White areas are pixels detected as porosity. Sample PA13 is the freshest  
 1101 sample of andesite, presenting moderate alteration of hornblende to montmorillonite at the  
 1102 bottom of the section (arrow 3), and silica and oxides abundance in the mesostase (arrows 1  
 1103 and 2). In sample PA4, intragranular alteration of hornblende crystals is underscored by  
 1104 montmorillonite and oxides in cleavage planes. Sample PA10.1 exhibits pervasive alteration  
 1105 of the mesostase (presence of montmorillonite, silica, and sulphide minerals) (arrows 1,2). In  
 1106 sample PA12, hornblende crystals are totally replaced by montmorillonite and iron oxides  
 1107 (arrow 1); carbonate veins are also detected (arrow 2). Sample PA11 is extremely altered;  
 1108 hornblende is totally replaced by silica and montmorillonite (arrow 3), and feldspars  
 1109 phenocrysts are partially dissolved, containing dissolution voids( arrow 2), which are partially  
 1110 filled with kaolinite and silica (arrow 1). In this sample, quartz grains remains unaltered.  
 1111



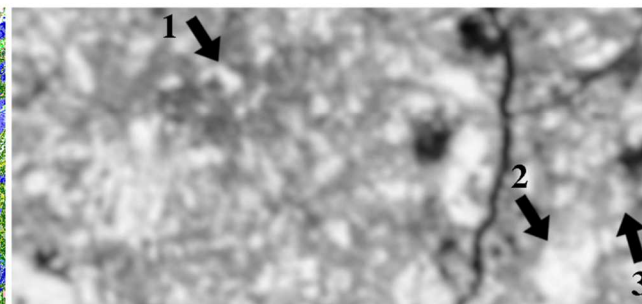
1112  
 1113 Figure 5: Correlation plot between the abundance of the clay phases identified by the  
 1114 QEMSCAN® system and the crystal lattice water proportions obtained from bulk-rock  
 1115 chemical analysis. Mt = montmorillonite and K = kaolinite.

1116  
 1117

- Quartz
- Magnetite/Hematite
- Magnetite/Hematite + Ti
- Ilmenite
- Anorthite
- Bytownite
- Labradorite
- Andesine
- Oligoclase
- Hornblende
- Montmorillonite
- Kaolinite
- Zircon
- Other silicates
- Apatite
- Sulfide mineral
- Calcite
- Ankerite
- Siderite
- Dolomite
- Rhodocrosite
- Glass
- Gypsum
- Other mineral
- Non identified



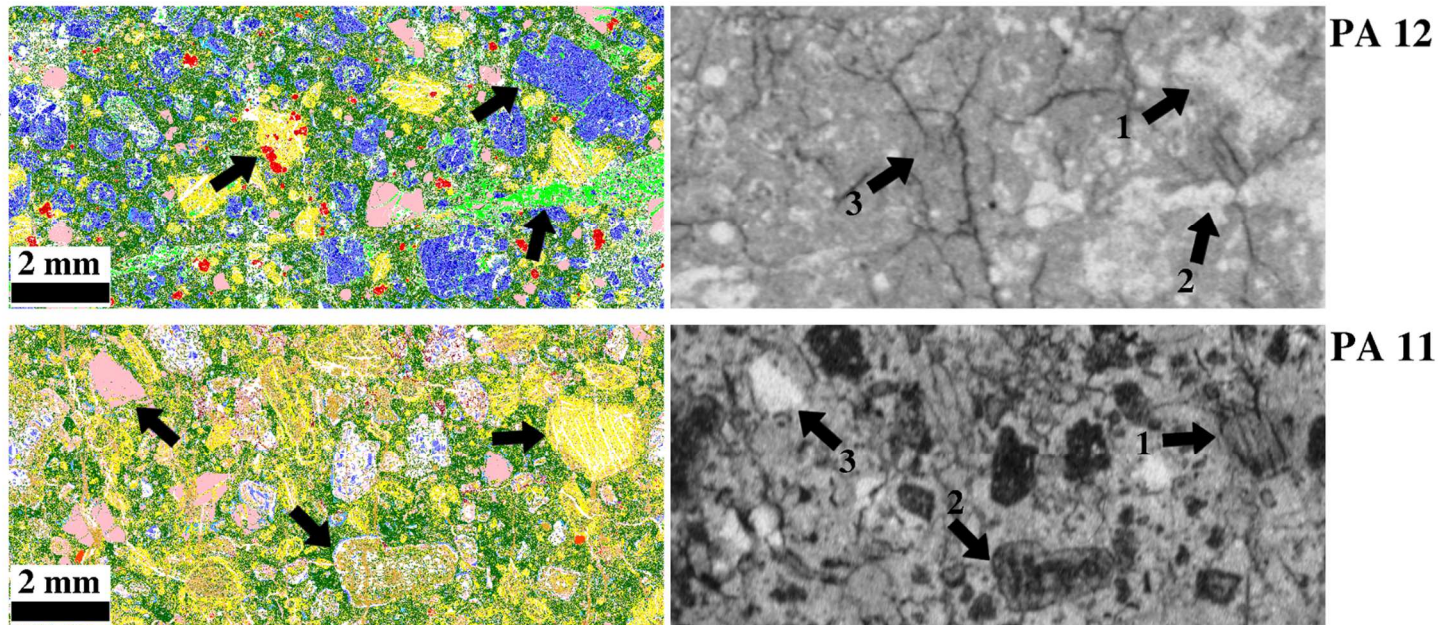
PA4



PA10.1



- Quartz
- Magnetite/Hematite
- Magnetite/Hematite + Ti
- Ilmenite
- Anorthite
- Bytownite
- Labradorite
- Andesine
- Oligoclase
- Hornblende
- Montmorillonite
- Kaolinite
- Zircon
- Other silicates
- Apatite
- Sulfide mineral
- Calcite
- Ankerite
- Siderite
- Dolomite
- Rhodocrosite
- Glass
- Gypsum
- Other mineral
- Non identified



1119

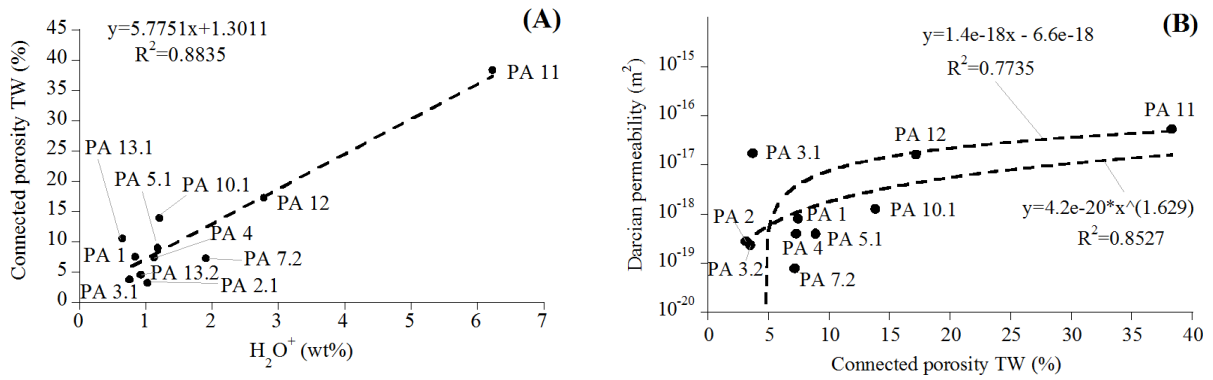
1120 Figure 6: QEMSCAN® Mineral maps (left) and related autoradiographs (right) from the <sup>14</sup>C-PMMA method of samples PA 13, PA 4, PA 10.1,  
 1121 PA 12 and PA 11. In autoradiographs, the darker the grey level is, the higher the porosity is. In the freshest sample (PA13) the most porous  
 1122 mineral is hornblende, partially replaced by montmorillonite in PA 13.1 side (arrow 1). In PA4 sample, porosity is well developed in hornblende  
 1123 cleavage planes (arrow 1), and corresponds to montmorillonite; feldspars remains lowly porous (arrow 2). In sample PA 10.1, low porosity area

1124 are initial feldspar phenocrysts (arrow 2), but are also in sulphide of pseudomorphosed hornblende (arrow1) and in carbonate cements.  
1125 Montmorillonite-rich areas and in a less extent mesostase present an higher porosity. In PA12, Feldspars remain unaltered and lowly porous  
1126 (arrow 1), as well carbonate. High porosity of pseudomorphosed hornblende cannot be differentiate from the porosity of the mesostase (arrow 3).  
1127 Sample PA11, which is the most affected by hydrothermal alteration, presents a totally different porosity pattern than sample PA12. In this  
1128 sample, quartz grains remains the only lowly porous mineral (arrow 3). The connected mesostase matrix is porous, but pseudomorphosed  
1129 hornblende (arrow 1) and altered/dissolved feldspars associated with dissolution voids (arrow 2) are more porous.

1130

1131

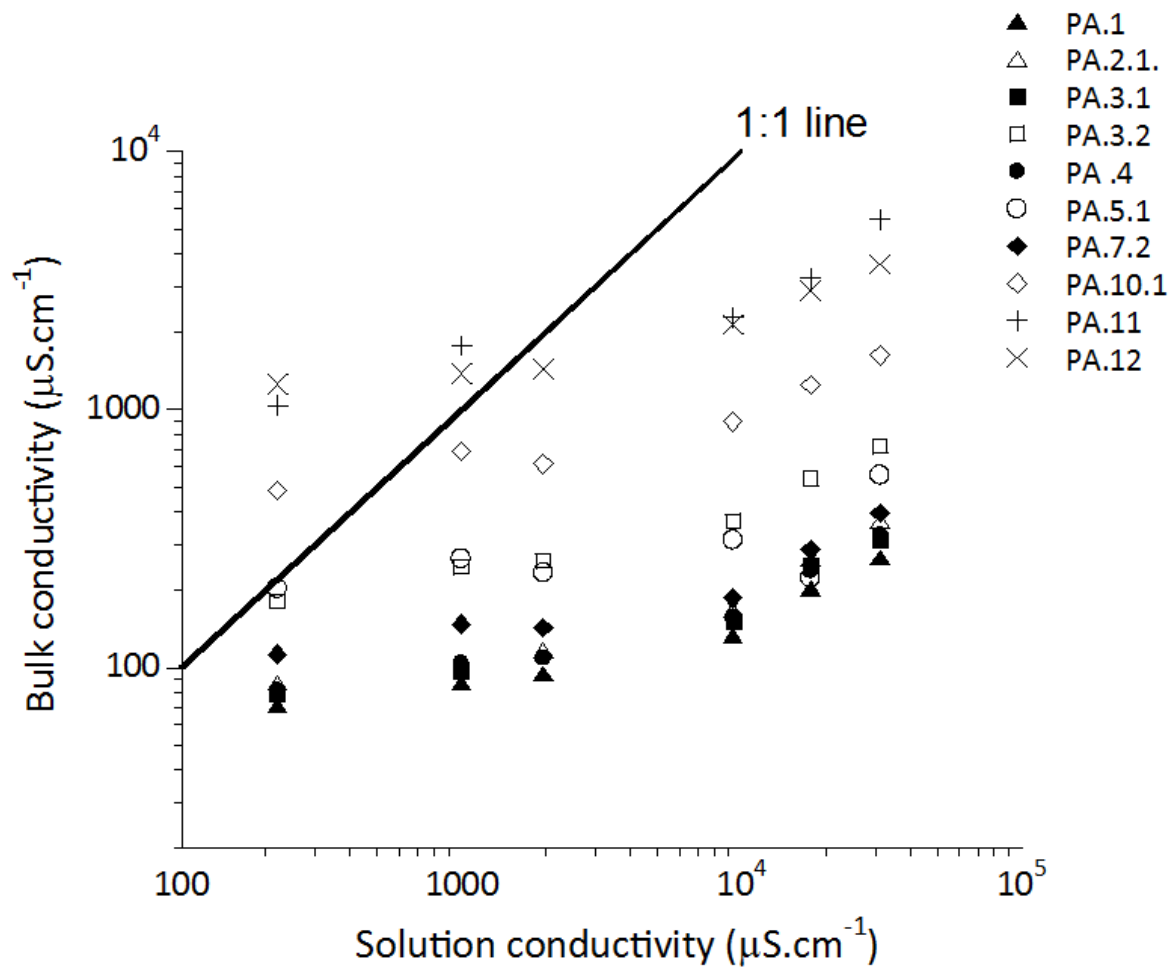
1132



1133 Figure 7: (A) Plot of the connected porosity of the samples against the structural water content  
1134 ( $H_2O^+$ ) value obtained with the triple weight (TW) method and from bulk-rock chemical  
1135 analysis. The  $H_2O^+$  values are used as indicators of the clay mineral abundances (see section  
1136 2.2). (B) Intrinsic permeability against the connected porosity.

1137

1138



1139

1140 Figure 8: Bulk conductivities versus conductivities of the solutions saturating the samples.

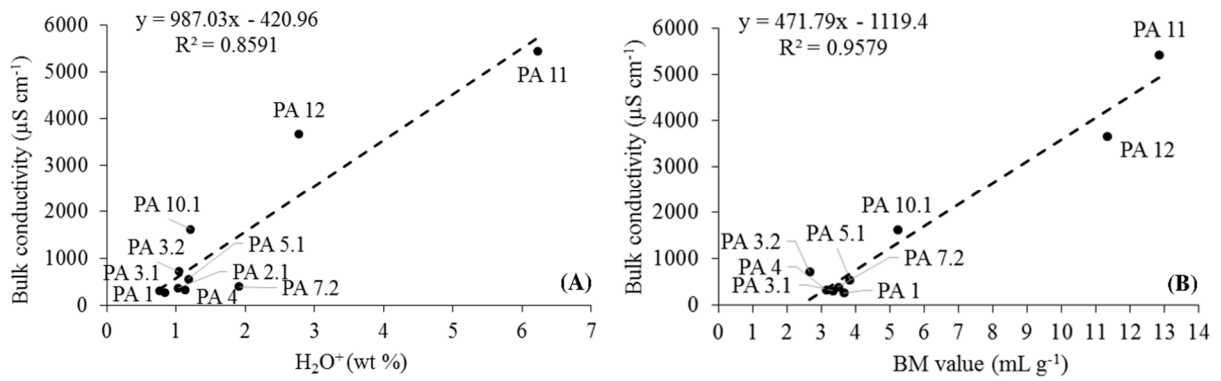
1141 The 1:1 line is used to estimate the isoconductivity point of each sample.

1142

1143

1144

1145



1146

1147 Figure 9: Correlation plots of the bulk conductivity measured for the samples saturated with  
1148 the 2 wt % NaCl solution depending on the structural water proportion ( $\text{H}_2\text{O}^+$ ) (A) and blue  
1149 methylene (BM) value (B).

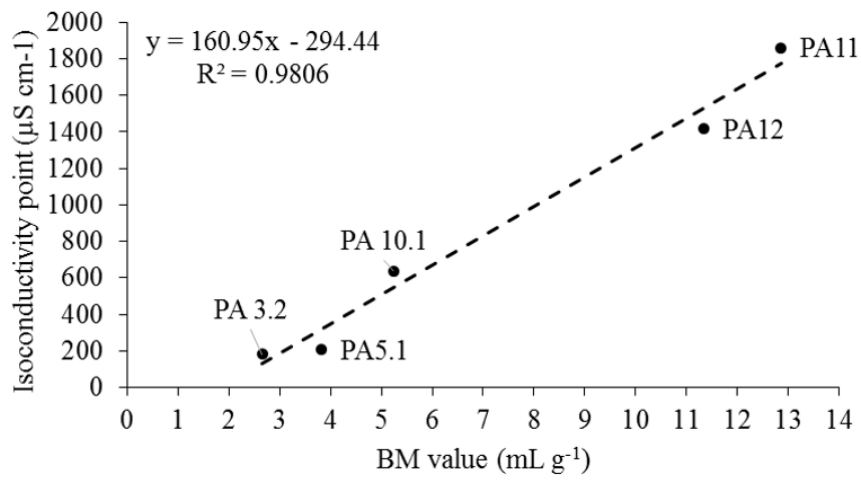
1150

1151

1152

1153

1154



1155

1156 Figure 10: Evolution of isoconductivity point depending on methylene blue value (BM).

1157

1158